ATLAS-COM-PHYS-99-029

Measurement of the LSP mass in supersymmetric models with R-parity violation

L Drage and M A Parker
Cavendish Laboratory, Madingley Rd, Cambridge CB3 0HE, UK
E-mail: `parker@hep.phy.cam.ac.uk`

28th October 1999

Abstract

This note contains an update to the analysis of the R-parity violating channel $\tilde{\chi}_1^0 \to qqq$ which was presented in the Physics TDR. The work forms part of the dissertation presented by L.Drage for the degree of PhD at Cambridge University. The text of the note is taken directly from the thesis. The full thesis can be found at http://www.hep.phy.cam.ac.uk/atlas/susy.

The Evaluation of Silicon Microstrip Detectors for the ATLAS Semiconductor Tracker and Supersymmetry Studies at the Large Hadron Collider

By
Lee Martin Drage
of
Trinity College

A dissertation submitted to the University of Cambridge
for the degree of Doctor of Philosophy
September 1999

Abstract

The ATLAS detector will surround one of the interaction points of the Large Hadron Collider at the European Centre for Particle Physics. The ATLAS Semiconductor Tracker (SCT) will provide precision tracking of charged particles using silicon microstrip detectors. The SCT silicon detectors must operate for at least 10 years in a high radiation environment, in a 2 T magnetic field and with non-normally incident particles.

The first half of this thesis investigates the performance of prototype detectors for the SCT using a 180 GeV/c pion beam. Two beam tests are documented. The first is used to compare the performance of two different silicon microstrip detector designs after detector irradiation to a fluence equivalent to 10 years of ATLAS operation. Detector efficiency, noise occupancy, precision and the charge division between detector strips are studied. The charge produced in a detector by incident pions is compared with the predictions of Landau theory. The second beam test compares the performance of an irradiated detector and an unirradiated detector of the selected SCT design in a magnetic field and with non-normally incident pions. The performance of detectors in both beam tests are found to mostly satisfy design specifications.

The accurate measurement of the momentum and position of charged particles will be essential when searching for new physics. Supersymmetry (SUSY) is the most theoretically favoured extension of the Standard Model, the current theory of fundamental particles and interactions. The majority of studies of the ATLAS potential to discover and investigate SUSY particles have assumed that a discrete symmetry, R-parity, is conserved. In this thesis, an R-parity and baryon number violating supergravity model is considered. A new version of the HERWIG Monte Carlo event generator which correctly incorporates R-parity violating vertices was used with ATLFAST, a particle level simulation of the ATLAS detector. An algorithm to measure three sparticle masses is presented. It is shown that the errors on these measurements are dominated by uncertainties in jet energy scale corrections.

5.1 Introduction

Supersymmetry (SUSY) is one of the most theoretically favoured extensions of Standard Model physics. This chapter investigates the possibility of discovering and measuring the mass of three SUSY particles in a baryon number violating scenario.

Chapter 1 discussed the concept of and motivations behind SUSY. The first part of this chapter describes a specific SUSY model and R-parity violation. The software tools used to generate SUSY events and to model the ATLAS detector performance are then discussed. The subsequent section describes the phenomenology of the SUSY scenario studied. Finally, the algorithm used to extract SUSY particle masses is discussed and results are presented.

5.2 Supersymmetry

5.2.1 The Minimal Supersymmetric Standard Model

The Minimal Supersymmetric Standard Model (MSSM) is the supersymmetric extension of the SM with minimal particle content. As in the SM, there are three families of leptons and quarks. Each of the SM fermions has a SUSY partner. Two complex Higgs doublets are needed to give mass to all fermions and there are five physical, spin-zero Higgs bosons: A, $H^{\pm}$, H^0 and h^0. These have spin-half superpartners called higgsinos. The superpartners of the $W^{\pm}$ and Z bosons mix with the higgsinos to give mass eigenstates: the charginos, $\tilde{\chi}^{\pm}_{1,2}$, and neutralinos, $\tilde{\chi}^0_{1,2,3,4}$.

The MSSM has 105 more free parameters than the Standard Model[1]. Phenomenological observations such as small CP violation and the lack of flavour changing neutral currents can be used to constrain the MSSM to 19 extra free parameters[2]. Another method of constraining the MSSM is to impose boundary conditions on parameters at the Grand Unification Theory (GUT) scale. One such constrained model, minimal supergravity or mSUGRA[3], involves gravitational interactions in SUSY breaking and automatically fulfils the phenomenological MSSM constraints[2]. The SUSY sector of mSUGRA is defined by the following boundary conditions[1]:

1. Gauge coupling strengths are equal at the GUT scale, M_U. This condition can be used to define M_U.
2. All gauginos have a mass $m_{\frac{1}{2}}$ at M_U.
3. Scalar sparticles have a mass m_0 at M_U.
4. All trilinear Higgs-sfermion-sfermion couplings are equal to A_0 at M_U.

In addition to m_0, $m_{\frac{1}{2}}$ and A_0, a further two input parameters are needed: β, the ratio of the vacuum expectation values of the two Higgs doublets and the sign of the SUSY conserving Higgs mass, μ. SUSY measurement and detection studies in ATLAS have concentrated on the six points in the mSUGRA parameter space listed in table 5.1. At each of these points, the lightest supersymmetric particle (LSP) is the χ^0_1.

mSUGRA point	m_0 (GeV)	$m_{\frac{1}{2}}$ (GeV)	A_0 (GeV)	$\tan\beta$	signμ
1	400	400	0	2.0	+
2	400	400	0	10.0	+
3	200	100	0	2.0	−
4	800	200	0	10.0	+
5	100	300	300	2.1	+
6	200	200	0	45	−

Table 5.1: The values of the mSUGRA parameters at the six LHC points[4, 5].

In the majority of ATLAS mSUGRA studies it is assumed that a discrete, multiplicative symmetry, R-parity, is conserved. The R quantum number of a particle is defined:

$$R = (-1)^{3B+L+2S} \tag{5.1}$$

where B, L and S are the baryon number, lepton number and spin of the particle[6]. Leptons and sleptons have $L = +1$, $B = 0$ and anti-leptons and anti-sleptons have $L = -1$, $B = 0$. Quarks and squarks have $L = 0$, $B = \frac{1}{3}$. It follows that SM particles have $R = 1$ and supersymmetric particles have $R = -1$. The R quantum number of a system of particles is the product of the individual particles' R quantum numbers. If R-parity is conserved, supersymmetric particles must be produced in pairs and the decay products of a SUSY particle must include an odd number of SUSY particles. A consequence of R-parity conservation is that the LSP is stable. In mSUGRA, the weakly interacting and neutral $\tilde{\chi}_1^0$ is the LSP and is assumed to leave the detector without interacting. A signature of R-parity conserving (RPC) mSUGRA is therefore missing transverse energy.

The conservation of R-parity is principally motivated by the long measured lifetime of the proton ($\tau(p \to e\pi) > 10^{32}$ years[7]). To understand this, it is easiest to consider first the terms added to the R-parity conserving MSSM superpotential to introduce R-parity violation (RPV)[6]:

$$W_{\not{R}_p} = \frac{1}{2}\lambda_{ijk} L_i L_j \bar{E}_k + \lambda'_{ijk} L_i Q_j \bar{D}_k + \frac{1}{2}\lambda''_{ijk} \bar{U}_i \bar{D}_j \bar{D}_k \tag{5.2}$$

In the SUSY Lagrangian, SM and SUSY particles are grouped together into lepton (L_i) and quark (Q_i) SU(2) doublet superfields and electron (E), down(D) and up(U) SU(2) singlet superfields. In equation 5.2, λ_{ijk}, λ'_{ijk} and λ''_{ijk} are Yukawa couplings between these superfields. The subscripts i, j and k are family indices. λ_{ijk} is antisymmetric under $i \leftrightarrow j$ and λ''_{ijk} is antisymmetric under $j \leftrightarrow k$. $W_{\not{R}_p}$ therefore adds $9 + 27 + 9 = 45$ free parameters to the MSSM superpotential.

Figure 5.1 shows examples of R-parity violating vertices introduced by the LLE, LQD and UDD terms in equation 5.2. The LLE and LQD terms are seen to violate lepton number conservation and the UDD term baryon number conservation.

Proton decay can occur, for example, via the $L_1 Q_1 \bar{D}_2$ and $\bar{U}_1 \bar{D}_1 \bar{D}_2$ vertices (figure 5.2). The lifetime of the proton has been measured to be greater than 10^{32} years

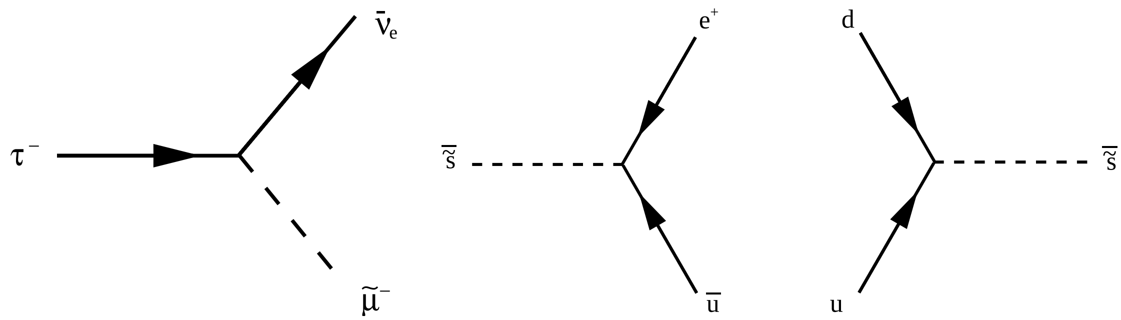

Figure 5.1: Examples of vertices introduced by the LLE, LQD and UDD terms in the R-parity violating superpotential.

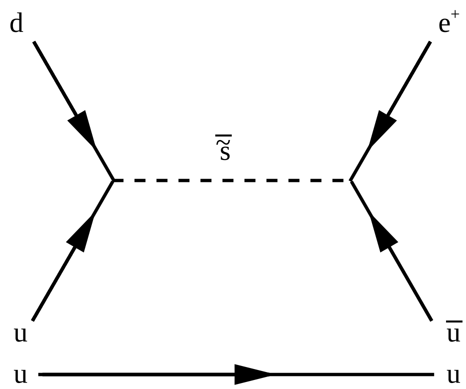

Figure 5.2: Proton decay via the R-parity violating $L_1Q_1\bar{D}_2$ and $\bar{U}_1\bar{D}_1\bar{D}_2$ vertices.

[7] and, for the given example, this imposes $\lambda'_{112}.\lambda''_{112} \lesssim 2.10^{-27}(\frac{\tilde{m}}{100\text{ GeV}})^2$[6] where $\tilde{m}$ is the mass of the exchanged strange squark. It is therefore natural to set one of the two Yukawa couplings to zero which is equivalent to conserving either lepton or baryon number. Both lepton and baryon number violation are needed for proton decay. RPV couplings are also constrained by limits on contributions, via the exchange of virtual SUSY particles, to other SM processes[6, 8].

RPV models consistent with current measurements can be constructed. In [6], it is argued that there are no theoretical or phenomenological reasons to favour RPC models over RPV models. It is therefore important to consider the discovery and measurement potential of both scenarios.

The difference in signature between RPV and RPC SUSY models depends on the strength of the RPV coupling. When RPV couplings are small compared to MSSM gauge couplings, the predominant consequence of R-parity violation is that the LSP can decay into SM particles. For RPV couplings of order 10^{-6} or smaller [9], the LSP has a sufficiently long lifetime to decay outside of the detector. The experimental signature is then identical to that of an RPC model. If RPV couplings are in the range $10^{-4} < \lambda, \lambda', \lambda'' < 10^{-2}$ [9], the LSP decays in the beam pipe and the missing energy signature, seen in RPC models, is not present.

If the RPV couplings and MSSM gauge couplings are of the same order of magnitude, RPV production processes and decays of particles heavier than the LSP become important. For a large λ'' coupling, for example, the branching fractions of RPC and RPV decays of a squark can be of the same order of magnitude.

5.3 Event simulation

For this analysis, events were generated using a private version of HERWIG. ATLFAST 2.0[10] was used to simulate the ATLAS detector.

5.3.1 Event generation

In June 1999, the publicly available release of HERWIG was version 5.9[11]. The release of a new version 6.1[12, 13] was planned later in the year. Whilst HERWIG 5.9 simulates just SM particles, versions from 6.0 upwards include the production and decay of MSSM particles. Version 6.1 also incorporates R-parity violating interactions.

The private version 6.0 used in this analysis includes all RPC SUSY processes and a subset of all RPV interactions. The limitations of this private version are described later in this section.

HERWIG generates SUSY events using a list of sparticle masses and decay modes. This information is produced using a modified version of ISASUSY[14]. ISASUSY iteratively solves the renormalisation group equations (RGE) of a given SUSY model. The RGEs are then used to evolve the free parameters of the model to find sparticle masses and couplings at the electroweak (EW) breaking scale. SUSY models implemented in ISASUSY include mSUGRA, non-universal SUGRA and gauge-mediated SUSY breaking (GMSB). The modified ISASUSY includes R-parity violating decays calculated for user defined values of the RPV Yukawa couplings (equation 5.2).

HERWIG factorises event generation into four subprocesses: Initial state radiation (ISR), the elementary hard process, final state radiation (FSR) and hadronisation. The colour flow through an event is recorded and used by HERWIG in hadronisation. In baryon number violating decays, the colour connection of an event is non-trivial and HERWIG 6.0 was modified to deal with such processes.

Not all RPV vertices are included in the version of HERWIG used for this analysis. The following processes are included:

1. All two-body squark and slepton decays
2. All three-body neutralino decays
3. The RPV production process $qq \rightarrow \tilde{\chi}_1^0 l^\pm$ via the LQD term (equation 5.2)

Three-body chargino and gluino RPV decays are not included and only the abovementioned RPV production process is implemented.

As discussed in the previous section, RPV production and RPV decays of particles other than the LSP are only important for large RPV couplings. This version of HERWIG is therefore adequate for studies where the RPV coupling is small and only the decay of the LSP is important.

When the analysis of this chapter was near completion, a revised version 6.02 of HERWIG became available. HERWIG 6.02 and HERWIG 6.0 differ in two ways relevant to this work. Firstly, the QCD renormalisation scale at which SUSY production is calculated was lowered in HERWIG 6.02, raising α_s and the total SUSY production cross section. The total cross section in the new version is in good agreement with ISAJET 7.40[14] and PROSPINO [15]. At mSUGRA point 5, the cross section is 20 % higher in the newer version of HERWIG than in HERWIG 6.0. Too much significance should not be placed on this 20% difference because the error on the total production cross section could be of the same order. Changing the parton distribution functions can change the SUSY cross section by 10 % and corrections of second order and higher, which are not implemented in HERWIG, may have a similar order effect.

The second difference in HERWIG 6.02 is the correction of an error in the sign of a chargino-neutralino-W coupling. With the correct sign, some cancellation occurs which reduces the associated neutralino and chargino production cross section. At point 5, the fractional production cross section is 14.6 % in HERWIG 6.0 and 7.7 % in HERWIG 6.02. All implicit signatures used in this analysis are from squark and gluino production and therefore the results presented here should be slightly pessimistic. The ratios of SUSY production rates quoted in this chapter are taken from HERWIG 6.0. The individual process production rates, however, have been scaled to give a total SUSY cross section which agrees with HERWIG 6.02.

5.3.2 ATLAS detector simulation

Detector simulation can be performed at three levels of sophistication. The most sophisticated simulations are full Monte Carlo studies which track individual particles through a detailed description of the detector geometry and material. Such simulations agree well with experiment but are slow and CPU intensive. At the other end of the spectrum are parton level simulations. These determine the topology of an event from its partons and leptons. There is, for example, no hadronisation of partons or taus.

Particle level simulations are a compromise between the fast but approximate parton level simulations and the accurate but slow full Monte Carlos. The stable, final state particles remaining after the hadronisation of quarks are the starting point of the simulation. In particle level simulations, all stable particles except neutrinos, muons and the SUSY LSP (if stable) are used to determine the energy deposited in a grid in (η, ϕ) space representing calorimeter cells. From a list of the energy in each cell, jets can be reconstructed. The energy deposited around an electron or muon can be used to determine whether it is isolated. Parameters such as the transverse momentum of an electron or the missing transverse momentum of an event are known from the particle generator and can be smeared to model detector inaccuracy as measured in test beams and full Monte Carlo simulations.

ATLFAST, a particle level simulation of the ATLAS detector, is described in more detail below.

Energy deposition in ATLFAST

In ATLFAST, calorimeter cells are of dimension $\Delta\eta \times \Delta\phi = 0.1 \times 0.1$ in the barrel ($|\eta| < 3$) and $\Delta\eta \times \Delta\phi = 0.2 \times 0.2$ in the forward regions ($3 < |\eta| < 5$). These cell sizes correspond approximately to the hadronic calorimeter cell sizes in the ATLAS detector[16]. From a list of stable particles generated by an event generator such as HERWIG, the energy deposited in each calorimeter cell is found. The effect on charged particles of the Inner Detector's solenoidal 2 T magnetic field is taken into account.

Calorimeter cell clustering

The next step is to search for clusters of calorimeter cells. A simple cone algorithm is used in this study and is described here. Firstly, calorimeter cells with an energy greater than 1.5 GeV are located for use as cluster initiator cells. The initiator cell with the highest energy is considered first. The total energy is found in all cells within a cone with half-angle $\Delta R = \sqrt{\Delta\eta^2 + \Delta\phi^2} = 0.4$ of the initiator cell. If this energy is greater than 10 GeV then the cells in the cone are identified as a cluster. The same procedure is then applied to the initiator cell with the next highest energy and not already included in a cluster. The treatment of overlapping cones is discussed in the next paragraph. The algorithm is repeated until all initiator cells have been considered. The position of a cluster is the energy weighted barycentre of the constituent cells.

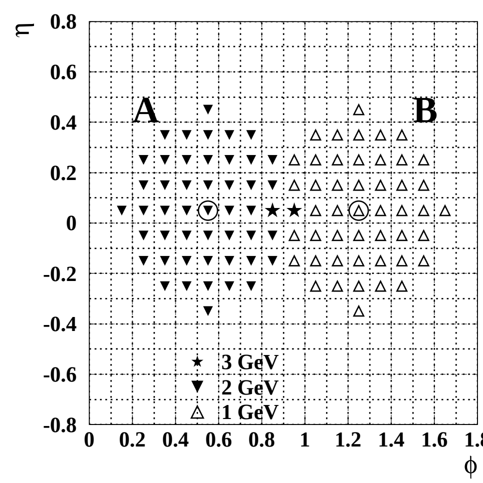

Figure 5.3: A simple simulation of the energy deposited in calorimeter cells by two overlapping jets.

In ATLFAST, it is possible to use the cone algorithm with and without energy sharing between overlapping clusters. The two algorithms are best explained using a diagram. Figure 5.3 shows the energy in $\Delta\eta \times \Delta\phi = 0.1 \times 0.1$ calorimeter cells for two hypothetical overlapping jets. Jet A and Jet B have energies of $E_A^{(T)} = 98$ GeV and $E_B^{(T)}$ =49 GeV and azimuthal angles $\phi_A^{(T)} = 0.5$ and $\phi_B^{(T)} = 1.2$. Assuming $\eta_A^{(T)} = \eta_B^{(T)} = 0$, the invariant

Method	E_a	E_b	$\Delta\phi$	m_{inv}
Correct energy sharing	98	49	0.700	47.52
No energy sharing	100	47	0.708	47.53
Energy sharing	98.1	48.9	0.708	48.02

Table 5.2: A comparison of the cone algorithm with and without energy sharing between overlapping clusters. The first row lists the true parameters of the jets. See the text for more details of the study.

mass of the two jets is $m_{inv}^{(T)} = \sqrt{2E_A^{(T)}E_B^{(T)}(1-\cos(\phi_A^{(T)}-\phi_B^{(T)}))} = 47.52$ GeV. For simplicity, the jet energy is spread uniformly throughout a cone of half-angle $\Delta R = 0.4$. In real jets, the energy distribution is peaked at the jet centre and only ∼90% of a hadronic shower is within $\Delta R = 0.4$ [17]. It is assumed that ATLFAST identifies the jet centre (marked with a circle) as the cluster initiator cell. The two cells with an energy of 3 GeV have contributions from both jets and are referred to here as shared cells.

The first step in the cone algorithms with and without energy sharing is the same. The initiator cell of cluster A has the highest energy and is considered first. The shared cells are associated with cluster A which therefore has an energy of 100 GeV. The cells not already used and within $\Delta R = 0.4$ of the initiator cell of jet B have a total energy of 47 GeV. The azimuthal angle of a cluster is given by:

$$\phi = \frac{\sum_i E_i \phi_i}{E} \tag{5.3}$$

where E_i and ϕ_i are the energy and azimuthal angle of an individual calorimeter cell and E is the total cluster energy. Associating the same cells with the cluster as in the energy calculation, the azimuthal angles of the clusters are $\phi_A = 0.507$ and $\phi_A = 1.215$. The two clusters have an invariant mass of $m_{inv} = 47.53$ GeV.

If the energy sharing option of ATLFAST is used, the energy of the clusters is then recalibrated. The energy in shared cells is divided between the two clusters in the ratio of their total energies as found without energy sharing. The position of the cluster, however, is not recalibrated. In the example, the recalibrated cluster energies are $E_A = 98.08$ GeV and $E_B = 48.91$ GeV. The invariant mass of the two clusters is then $m_{inv} = 48.02$ GeV.

The results of the two approaches are summarised in table 5.2. When energy sharing is used, the cluster energies are nearer the jet energies than without. The error in the invariant mass, however, is larger with energy sharing. This effect was found to be more pronounced when there is more overlap between cones. A similar increase in the invariant mass of three overlapping clusters was found.

In this study, the invariant mass of three jets is used. The jets are often close together and energy sharing between clusters is not used. This choice is fairly academic anyway since precision mass measurements would not be performed using a simple cone algorithm. The use of clustering algorithms is discussed in more detail at the end of this chapter.

Isolated leptons

Once ATLFAST has identified clusters, the list of generated particles is searched for photons, muons and electrons within the pseudorapidity range of the Inner Detector ($|\eta| < 2.5$) and with transverse momentum greater than approximately 5 GeV. The four-momentum of isolated muons, photons and electrons is smeared according to an energy, luminosity and particle dependent function determined by full simulation[18]. Low luminosity ($L = 10^{33}$ cm^{-2} s^{-1}) parameterisations have been used throughout this analysis. The calorimeter clusters of electrons and photons are identified by comparing cluster positions with the smeared coordinates of the generated particle. A photon, electron or muon is labelled as isolated if:

- The separation in (η,ϕ) between the smeared coordinates of the particle and the nearest cluster not associated with the particle is greater than $\Delta R = 0.4$.
- The total energy in calorimeter cells within $\Delta R = 0.2$ of the particle is less than 10 GeV greater than the smeared transverse momentum of the generated particle.

Jets and jet flavour tagging

The calorimeter clusters not associated with isolated photons, electrons or muons and with an energy greater than 10 GeV are labelled as jets. The jet energies are smeared according to an energy and luminosity dependent function. A jet is initially labelled as a b-jet or c-jet if it is within $\Delta R < 0.2$ of a generated b-quark or c-quark with $p_T > 5$ GeV and $|\eta| < 2.5$.

b-tagging efficiency	Rejection factor	
ϵ_b(%)	u,d,s,g jets (r_q)	c jets (r_c)
33	1400±400	22.9±2.0
43	220±30	10.8±0.6
53	91±7	6.7±0.3
64	32±2	4.2±0.1

Table 5.3: b-tagging efficiencies and mis-tagging rejection factors implemented in ATLFAST

In actual experiments, totally efficient b-tagging is unachievable and there is a finite chance of mis-tagging other flavour jets as b-jets. Table 5.3 lists four different b-tagging efficiencies and the corresponding mis-tagging rejection factors available in ATLFAST. These numbers were found using full Monte Carlo simulations in [19]. The rejection factors are, in fact, a function of the transverse momentum of the jet and the numbers shown are an average over all p_T (see [10]). ATLFAST simulates realistic b-tagging performance by only tagging ϵ_b of jets matched with a b-jet. $1/r_c$ and $1/r_q$ of jets matched with c-quarks and other flavour quarks respectively are mis-tagged as b-jets[a].

[a] In reality, the rejection factor against mis-tagging gluon jets is worse than for light quark jets because the decays of a gluon into $b\bar{b}$ and $c\bar{c}$ have finite branching ratios of 4% and 6% respectively.

The missing transverse momentum of an event is calculated by ATLFAST using the energy and position of calorimeter clusters and cells.

A good agreement between full Monte Carlo simulations and ATLFAST has been demonstrated in $A/H \to \tau\tau$ and $h \to b\bar{b}$ decay channels[20].

5.4 A brief literature survey

Some work has already been done on the discovery potential of R-parity violating SUSY at the LHC. In [21], it is assumed that RPC SUSY will be searched for first. The paper therefore investigates the possibility of extracting an implicit RPV signature from cuts designed to detect RPC SUSY. It is found that after one year of running the LHC will be able to detect spartons from RPV SUSY with masses of up to 1 TeV.

The implications of a non-zero λ coupling (see equation 5.2) is explored in [9]. Again, it is found that a signal of RPV mSUGRA would be visible over a large region of parameter space. If the LSP decays into only electrons and muons, precision measurements of the free parameters of the model can be made.

The consequences of a non-zero λ'' coupling are investigated in [22] using the FORCE datacard of ISAJET. The study focuses on mSUGRA point 5 but also briefly considers the other LHC mSUGRA points. At point 5, it is shown that an inclusive signature can be used to detect the presence of new physics. Some explicit signatures are also investigated and the following mass measurements are made:

- LSP mass, $m(\tilde{\chi}_1^0) = 122 \pm 3.1$(stat)$\pm$1.3(syst) GeV
- Light right-slepton mass, $m(\tilde{l}_R) = 157 \pm 5.1$(stat)$\pm$1.6(syst) GeV
- $\tilde{\chi}_2^0$ mass, $m(\tilde{\chi}_2^0) = 233 \pm 4.1$(stat)$\pm$2.3(syst) GeV
- Light left-squark mass, $m(\tilde{q}_L) = 664 \pm 30$(stat)$\pm$7(syst) GeV

Very tight kinematic cuts are used in this analysis and the width of the obtained $\tilde{\chi}_1^0$ mass peak is largely defined by the cuts. The cone and mulguisin[23] clustering algorithms are compared. Neither is found to be significantly better than the other for the analysis presented.

5.5 LHC mSUGRA point 5 with non-zero λ''_{212}

5.5.1 Motivations for choosing point 5 and non-zero λ''_{212}

This analysis is a more detailed study of one part of the work presented in [22]. The results in this chapter are therefore for mSUGRA point 5 (table 5.1). In RPC models, the stable $\tilde{\chi}_1^0$ is a good candidate for weakly interacting massive particles (WIMPs) which may form some of the dark matter in the universe. The parameters of point 5 were originally chosen to be consistent with cosmological density measurements [24] inferred from COBE observations [25]. Of course, with R-parity not conserved, this argument is

ijk	Jet flavour	λ''	ijk	Jet flavour	λ''
112	uds	10^{-6}	223	csb	1.25
113	udb	10^{-5}	312	tdc	0.43
123	usb	1.25	313	tdb	0.43
212	cds	1.25	323	tsb	0.43
213	cdb	1.25			

Table 5.4: Upper limits (2σ) on individual λ'' couplings[6].

no longer valid. Point 5 does, however, offer a variety of interesting SUSY signatures to study.

Again for consistency with [22], the only non-zero RPV coupling in this analysis is λ''_{212}. The current limits on all λ'' couplings are shown in table 5.4. Only the λ''_{112} and λ''_{113} couplings are strongly constrained. In this analysis, a non-zero λ''_{212} allows the decay $\tilde{\chi}^0_1 \rightarrow cds$ (figure 5.4). The invariant mass of the jets from the c, d and s-quarks provide a measure of the $\tilde{\chi}^0_1$ mass. Except where jet-flavour tagging is used, the $\tilde{\chi}^0_1$ mass reconstruction in scenarios with non-zero λ''_{123}, λ''_{213}, λ''_{223}, λ''_{112} and λ''_{113} will be similar. The use of b-tagging is investigated in this analysis but is found to offer little advantage. The methods presented here can, therefore, be equally applied to scenarios with a different non-zero λ''.

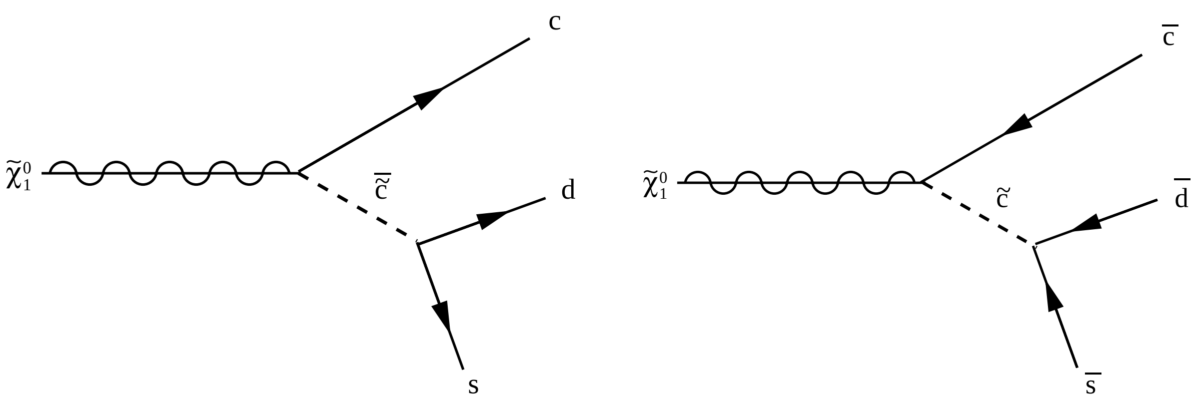

Figure 5.4: The R-parity violating decays of the LSP for $\lambda_{212} \neq 0$.

In [22], ISAJET 7.31 was used as the event generator. R-parity violating vertices are not implemented in ISAJET 7.31 but it is possible to force the decay of a stable particle. To simulate a small but non-zero λ''_{212}, the $\tilde{\chi}^0_1$ was forced to decay into cds or $\bar{c}\bar{d}\bar{s}$. The version of HERWIG used for the analysis presented here is only valid for small λ''. For this reason, and to be compatible with previous work, a value of 0.005 was chosen for λ''_{212}.

The choice of $\lambda''_{212} = 0.005$ is supported by figures 5.5a-b. In figure 5.5a, the branching fraction of the RPC decay $\tilde{d}_R \rightarrow \tilde{\chi}^0_1 d$ and the RPV decay $\tilde{d}_R \rightarrow \bar{c}\bar{s}$ are plotted against λ''_{212}. At $\lambda''_{212} = 0.005$, the $\tilde{d}_R$ decay is dominated by the RPC channel. This value of the coupling is therefore within the limits of the version of HERWIG used. In figure 5.5b,

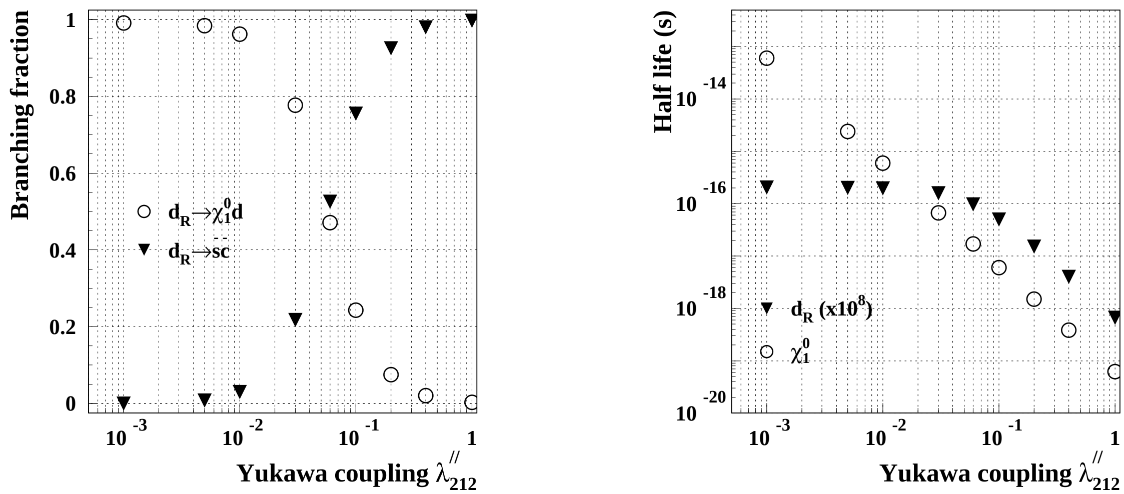

(a) (b)

Figure 5.5: **(a)** Branching fraction of RPC and RPV decays of $\tilde{d}_R$ plotted against λ''_{212}. **(b)** The lifetime of the $\tilde{\chi}^0_1$ and $\tilde{d}_R$ plotted against λ''_{212}.

the lifetime of the $\tilde{\chi}^0_1$ and $\tilde{d}_R$ are plotted against λ''_{212}. At $\lambda''_{212} = 0.005$, the $\tilde{\chi}^0_1$ has a lifetime of 2.4×10^{-15} s and thus decays in the beam pipe.

5.5.2 Characteristics of RPV point 5

Table 5.5 shows sparticle masses and principal decay modes for mSUGRA point 5 with $\lambda''_{212} = 0.005$. Squarks have masses of around 650 GeV and the gluino has a mass of 733 GeV. Sleptons are considerably lighter than spartons with a mass of approximately 200 GeV. The LSP is the $\tilde{\chi}^0_1$ with a mass of 121.5 GeV. The lightest Higgs in this scenario is the h^o. With a mass of 94.3 GeV it is just beyond the current Higgs lower mass limit of 79.6 GeV [26] and should be discovered by LEP 2 [27].

SUSY production cross sections for this point are listed in table 5.6. The total SUSY production cross section at point 5 was found to be 21.89 pb using HERWIG 6.02. Sparton production is seen to dominate in this mSUGRA model.

Figure 5.6 illustrates the dominant sparton decay chains of mSUGRA point 5. The $\tilde{q}_L$ decay chain studied in this analysis is shown in figure 5.6a. Two opposite sign, same family (OSSF) fermions are produced, the invariant mass distribution of which has a sharp upper edge at $m_{ll}^{(max)} = 109.1$ GeV. The $\tilde{\chi}^0_1$, right-slepton and $\tilde{\chi}^0_2$ masses are related to $m_{ll}^{(max)}$ by (Appendix A):

$$m_{ll}^{(\mathrm{max})} = m_{\tilde{\chi}^0_2}\sqrt{1 - \frac{m^2_{\tilde{l}_R}}{m^2_{\tilde{\chi}^0_2}}}\sqrt{1 - \frac{m^2_{\tilde{\chi}^0_1}}{m^2_{\tilde{l}_R}}} \quad (5.4)$$

Parent	Mass (Gev)	Decay products	b.f.
$\tilde{u}_L(\tilde{c}_L)$	654.1	$\tilde{\chi}_1^+ d(s)$	0.653
		$\tilde{\chi}_2^0 u(c)$	0.330
$\tilde{d}_L(\tilde{s}_L)$	657.2	$\tilde{\chi}_1^- u(d)$	0.642
		$\tilde{\chi}_2^0 d(u)$	0.314
$\tilde{b}_1$	600.3	$\tilde{\chi}_1^- t$	0.414
		$\tilde{\chi}_2^0 b$	0.284
		$\tilde{t}_1 \mathrm{W}^-$	0.274
$\tilde{t}_1$	459.6	$\tilde{\chi}_1^+ b$	0.643
		$\tilde{\chi}_1^0 t$	0.231
		$\tilde{\chi}_2^0 t$	0.126
$\tilde{u}_R$	631.0	$\tilde{\chi}_1^0 u$	0.991
$\tilde{d}_R(\tilde{s}_R)$	628.4	$\tilde{\chi}_1^0 d(s)$	0.984
		$\bar{c}\ \bar{s}(\bar{d})$	0.008
$\tilde{c}_R$	631.0	$\tilde{\chi}_1^0 c$	0.989
		$\bar{s}\ \bar{d}$	0.002
$\tilde{b}_2$	628.8	$\tilde{\chi}_1^0 b$	0.675
		$\tilde{t}_1 \mathrm{W}^-$	0.150
$\tilde{t}_2$	670.7	$\tilde{t}_1 \mathrm{Z}^0/\gamma^*$	0.340
		$\tilde{\chi}_1^+ b$	0.265
h^0	94.3	$b\ \bar{b}$	0.882
H^0	611.7	$t\ \bar{t}$	0.946
A^0	606.8	$t\ \bar{t}$	0.921
H^+	612.2	$t\ \bar{b}$	0.968

Parent	Mass (Gev)	Decay products	b.f.
$\tilde{g}$	732.9	$\tilde{b}_1\bar{b}$, $\tilde{t}_1\bar{t}$ +c.c.	0.075
		$\tilde{d}_R\bar{d}$, $\tilde{s}_R\bar{s}$ +c.c.	0.049
		$\tilde{b}_2\bar{b}$ +c.c.	0.48
		$\tilde{u}_R\bar{u}$, $\tilde{c}_R\bar{c}$ +c.c.	0.047
		$\tilde{u}_L\bar{u}$, $\tilde{c}_L\bar{c}$ +c.c.	0.029
		$\tilde{d}_L\bar{d}$, $\tilde{s}_L\bar{s}$ +c.c.	0.027
$\tilde{e}_L^\pm(\tilde{\mu}_L^\pm)$	238.8	$\tilde{\chi}_1^0 \mathrm{e}^\pm(\mu^\pm)$	0.940
		$\tilde{\chi}_1^\pm \nu_e(\nu_\mu)$	0.042
$\tilde{\tau}_1^\pm$	156.8	$\tilde{\chi}_1^0 \tau^\pm$	1.000
$\tilde{\nu}_e(\tilde{\nu}_\mu)$	238.8	$\tilde{\chi}_1^0 \nu_e(\nu_\mu)$	1.000
$\tilde{e}_R^\pm(\tilde{\mu}_R^\pm)$	157.2	$\tilde{\chi}_1^0 \mathrm{e}^\pm(\mu^\pm)$	1.000
$\tilde{\tau}_2^\pm$	238.9	$\tilde{\chi}_1^0 \tau^\pm$	0.939
$\tilde{\chi}_1^0$	121.5	$\bar{c}\ d$	0.5
		$c\ d$	0.5
$\tilde{\chi}_2^0$	233.0	$\tilde{\chi}_1^0 h^0$	0.646
		$\tilde{\tau}_1^\pm \tau^\mp$+c.c.	0.060
		$\tilde{e}_R^\pm \mathrm{e}^\mp$, $\tilde{\mu}_R^\pm \mu^\mp$ + c.c.	0.046
$\tilde{\chi}_1^\pm$	232.0	$\tilde{\chi}_1^0 \mathrm{W}^\pm$	0.897
		$\tilde{\tau}_1^\pm \nu_\tau$	0.066
$\tilde{\chi}_2^\pm$	520.1	$\tilde{\chi}_2^0 \mathrm{W}^\pm$	0.292
		$\tilde{\chi}_1^\pm \mathrm{Z}^0/\gamma^*$	0.258
		$\tilde{\chi}_1^\pm h^0$	0.202

Table 5.5: Sparticle masses and their principal branching fractions (b.f.) at mSUGRA point 5 with the R-parity violating coupling, $\lambda''_{212} = 0.005$. Several decay products listed on one line indicates that the branching ratio is the same for each decay i.e. $\Gamma_f(\tilde{g} \rightarrow \tilde{b}_1\bar{b}) = \Gamma_f(\tilde{g} \rightarrow \tilde{t}_1\bar{t}) = 0.075$. Charge conjugate has been abreviated as c.c.

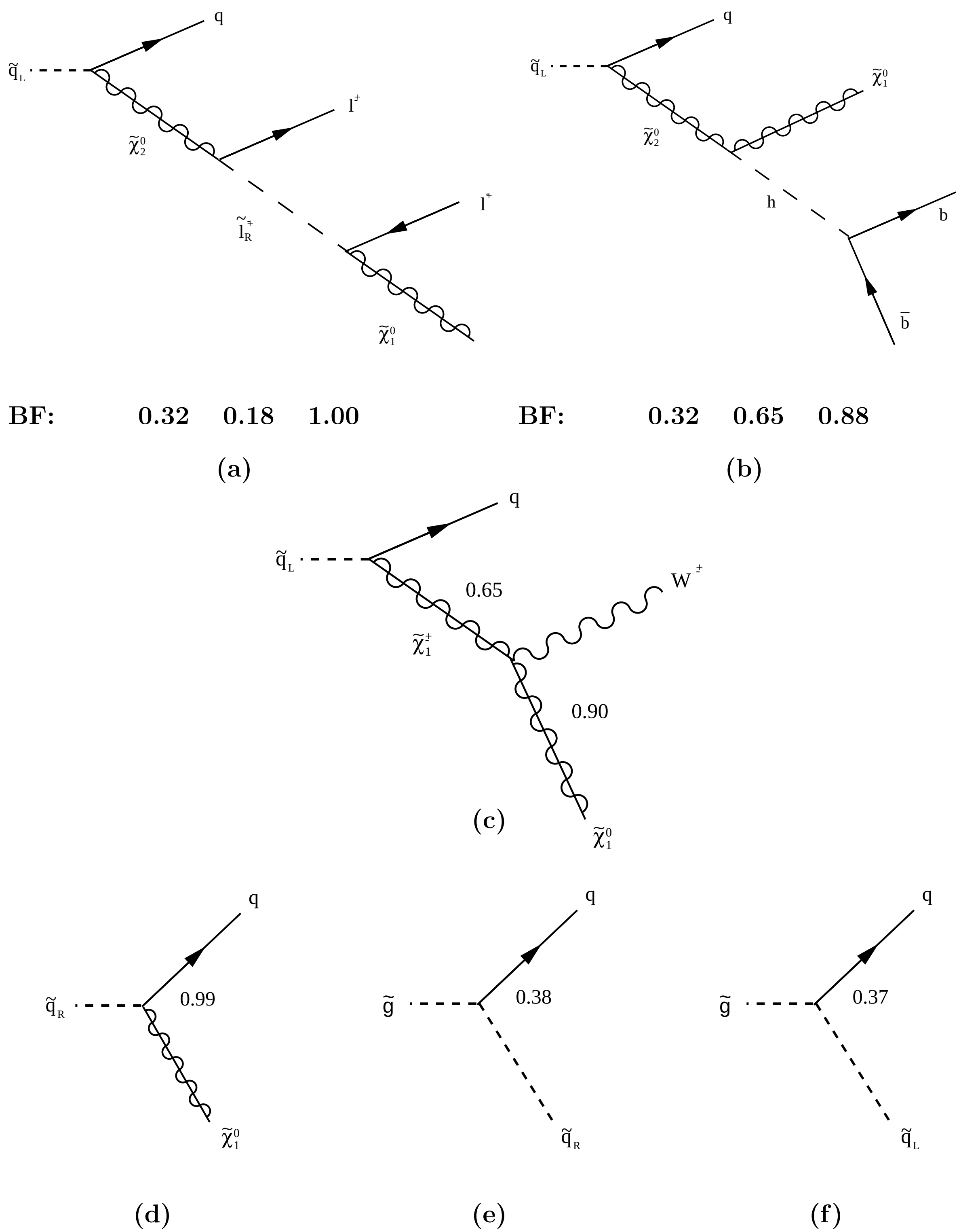

Figure 5.6: Important sparton decay chains at mSUGRA point 5. The RPV decay of the $\tilde{\chi}_1^0$ into c, d and s-quarks is not shown. The branching fractions for the vertices of each diagram are shown below (a-b) or in the angle of the vertices (c-f). These branching fractions are for $q = u, d, s, c, b$ and $l = e, \mu$ in (a), (b) and (f) and $q = u, d, s, c$ in (c), (e) and (d). The combined branching fractions of the decay chains are (a) 0.059 (b) 0.183 (c) 0.588.

Production products	Production cross section		Events in 3 years
	Fractional	(pb)	
$\tilde{q}_R\tilde{q}_R$	0.111 ± 0.001	2.43	77760
$\tilde{q}_L\tilde{q}_L$	0.132 ± 0.001	2.89	92480
$\tilde{q}_R\tilde{q}_L$	0.064 ± 0.001	1.40	44800
$\tilde{q}_R\tilde{g}$	0.232 ± 0.001	5.08	162560
$\tilde{q}_L\tilde{g}$	0.213 ± 0.001	4.66	149120
$\tilde{g}\tilde{g}$	0.097 ± 0.001	2.12	67840
$\tilde{l}\,\tilde{l}$	0.005 ± 0.000	0.11	3520
$\tilde{\chi}^{\pm}_{1,2}$, $\tilde{\chi}^0_{1,2,3,4}$	0.146 ± 0.001	3.20	102400
Total	1.0	21.89	$\sim 700 \times 10^3$

Table 5.6: SUSY production cross sections at mSUGRA point 5. The fractional cross sections were found using HERWIG 6.0. The absolute cross sections have been normalised to give a total SUSY production cross section of 21.89 pb, as found using HERWIG 6.02. The right-most column of the table lists the number of events expected after three years of low luminosity running ($\int dt\, L = 3.2 \times 10^4$ pb^{-1}).

In the RPC scenario, the $\tilde{\chi}^0_1$ leaves the detector without interacting and its mass can not be measured directly. Equation 5.4 and other variables sensitive to SUSY parameters must be combined to find $m_{\tilde{\chi}^0_1}$, $m_{\tilde{\chi}^0_2}$ and $m_{\tilde{l}_R}$ [24]. In the RPV scenario of this analysis, the $\tilde{\chi}^0_1$ mass can be measured directly. In principle, the $\tilde{l}_R$, $\tilde{\chi}^0_2$ and $\tilde{q}_L$ masses can then be found since all SM products of the decay chain can be detected.

The three-body decay $\tilde{\chi}^0_2 \to \tilde{\chi}^0_1 l^+ l^-$ has the same final state particle content as the $\tilde{\chi}^0_2$ decay in figure 5.6a. In this case, the edge of the OSSF lepton pair invariant mass distribution $m_{ll}^{(\max)} = m_{\tilde{\chi}^0_2} - m_{\tilde{\chi}^0_1}$. At point 5, $\Gamma(\tilde{\chi}^0_2 \to \tilde{l}^{\pm} l^{\mp})/\Gamma(\tilde{\chi}^0_2 \to \tilde{\chi}^0_1 l^+ l^-) = 46$ and this decay is not a significant background.

If R-parity is conserved, the $\tilde{\chi}^0_2 \to \tilde{\chi}^0_1 h^o \to \tilde{\chi}^0_1 b\bar{b}$ decay (figure 5.6b) can be used to find the mass of the h^o[24]. After three years of running, a clear peak in the $b\bar{b}$ invariant mass is seen. In baryon number violating scenarios, the signal peak is difficult, or impossible, to extract because of the increased jet multiplicity [22]. For most non-zero λ'', at least one b-quark or c-quark is produced in the $\tilde{\chi}^0_1$ decay. The increased number of b-jets and mis-tagged c-jets introduces a large combinatorial background.

The left-handed squarks that do not decay into $\tilde{\chi}^0_2 q$ mostly decay via $\tilde{q}_L \to \tilde{\chi}^{\pm}_1 q \to \tilde{\chi}^0_1 W^{\pm} q$ (figure 5.6c). This decay chain is less useful for finding model parameters. When the W decays hadronically (bf=67.9% [7]) the two jets are difficult to separate from at least eight other jets. In the case of the W decaying leptonically, the production of a neutrino prevents the determination of the W momentum.

Right handed squarks nearly always decay into $\tilde{\chi}^0_1 q$ (figure 5.6d). Gluinos decay into $\tilde{q}_R q$ and $\tilde{q}_L q$ with approximately equal probability (figures 5.6e-f).

5.6 Measuring the $\tilde{\chi}_1^0$ mass at RPV point 5

5.6.1 Introduction

In the RPV model of this analysis, the $\tilde{\chi}_1^0$ decays into three quarks. This section develops an algorithm to identify the jets from these quarks and find their invariant mass, thus measuring the $\tilde{\chi}_1^0$ mass. In this algorithm, a number of cuts are made on the data to reduce backgrounds from SUSY and SM processes. Three measures of the effectiveness of a set of cuts are presented in section 5.6.2. These are used in subsequent sections to optimise the algorithm.

In the RPV scenario being studied, two $\tilde{\chi}_1^0$s are produced in nearly all events. The $\tilde{\chi}_1^0$ with the highest transverse momentum is referred to as the hard $\tilde{\chi}_1^0$ and the other the soft $\tilde{\chi}_1^0$. The mean transverse momenta of the hard and soft $\tilde{\chi}_1^0$s from all SUSY production processes were measured at the generator level to be 292 GeV and 157 GeV.

5.6.2 Effectiveness of cuts

The effectiveness of the algorithm used to separate the $\tilde{\chi}_1^0$ mass peak from backgrounds is quantified by three variables: the precision of the mass measurement, the bias of the mass peak and the reconstruction efficiency.

The precision of the mass measurement is defined to be the error on the mean of a Gaussian fitted to the data. The reconstructed mass distribution has a shoulder at around 150 GeV and so the Gaussian fit is performed over the range $0 < m_{jjj} < 140$ GeV.

The bias of the mass peak is defined as $b_m = m_{jjj} - m_{\tilde{\chi}_1^0}$ where m_{jjj} is the reconstructed $\tilde{\chi}_1^0$ mass and $m_{\tilde{\chi}_1^0}$ is the true $\tilde{\chi}_1^0$ mass (121.5 GeV at point 5).

Two reconstruction efficiencies will be used in this chapter. The reconstruction efficiency ϵ_1 is the fraction of generated events in which one well matched $\tilde{\chi}_1^0$ is reconstructed. The reconstruction efficiency ϵ_2 is the fraction of generated events in which two well matched $\tilde{\chi}_1^0$s are reconstructed. Two $\tilde{\chi}_1^0$s are generated in nearly all events. A reconstructed $\tilde{\chi}_1^0$ is defined to be well matched if the spatial separation between it and the HERWIG generated $\tilde{\chi}_1^0$ is small. The separation between a reconstructed $\tilde{\chi}_1^0$ at $(\eta_{recon}, \phi_{recon})$ and the generated $\tilde{\chi}_1^0$ at $(\eta_{parton}, \phi_{parton})$ is measured using:

$$\Delta R_{mat} = \sqrt{(\phi_{parton} - \phi_{recon})^2 + (\eta_{parton} - \eta_{recon})^2} \tag{5.5}$$

To determine what constitutes a well matched $\tilde{\chi}_1^0$, the $\tilde{\chi}_1^0$ mass peak was found, using the algorithm presented later in this chapter, with different upper limits on ΔR_{mat}. As the combinatorial background is removed by requiring better matching, the $\tilde{\chi}_1^0$ mass peak width approaches a minimum due to jet measurement errors alone. The width of the hard $\tilde{\chi}_1^0$ mass peak reaches a plateau value of approximately 10.0 GeV at $\Delta R_{mat}^{(a)} < 0.03$. The soft $\tilde{\chi}_1^0$ mass peak width is at a minimum below $\Delta R_{mat}^{(b)} < 0.05$. The hard and soft $\tilde{\chi}_1^0$s are therefore defined to be well matched if $\Delta R_{mat} < 0.03$ and $\Delta R_{mat} < 0.05$ respectively.

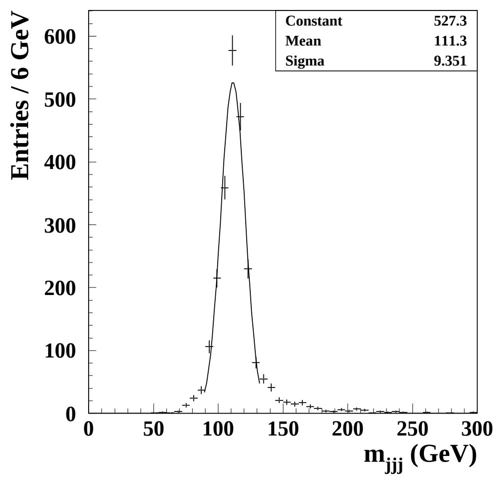

Figure 5.7: The mass distribution of reconstructed $\tilde{\chi}_1^0$s well matched spatially to the HERWIG generated sparticle. The jet combinations used to generate the plot were selected using the "Jet cuts" ($n_{jet}^{(max)} = 10$) presented in section 5.6.4 and the ΔR_{mat} cuts described in the text. Simulated data for three years of running were used. There are 2080 events in the peak.

The mass peak for well matched $\tilde{\chi}_1^0$s (both hard and soft) is plotted in figure 5.7. Not all energy deposited by softer jets is within a cone of width $\Delta R = 0.4$. For this reason, the centre of the matched $\tilde{\chi}_1^0$ mass peak is 8% lower than the true mass of 121.5 GeV. This plot indicates that the bias of a mass peak in which there is minimal background should be $b_m \approx -10$ GeV.

5.6.3 The data sample

A data sample of 7×10^5 simulated SUSY events is used to determine sparticle masses. This data set corresponds to three years of low luminosity running ($L = 10^{33}$ cm^{-2} s^{-1}, $\int dtL = 3.2 \times 10^4$ pb^{-1}). The ratios in which different SUSY particles are generated were given in table 5.6. The SUSY data sample does not include any events in which only SM particles are produced.

5.6.4 Cuts against SUSY backgrounds

The cuts used to extract a $\tilde{\chi}_1^0$ mass peak from SUSY events can be classified as jet, lepton or b-tagging cuts.

Jet cuts

The principal difficulty in measuring the $\tilde{\chi}_1^0$ mass is identifying jets from the $\tilde{\chi}_1^0$ decay. It is instructive to consider the jet multiplicity in events.

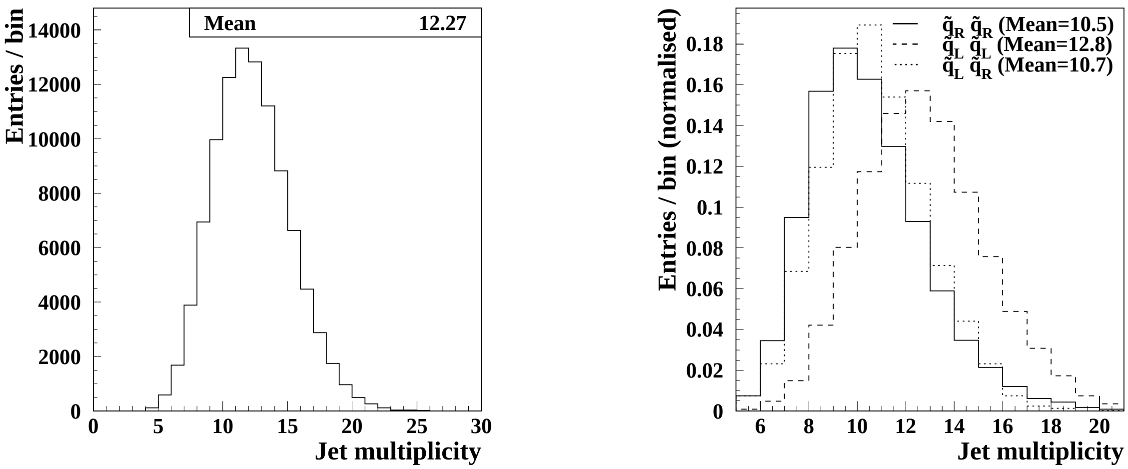

(a) (b)

Figure 5.8: The jet multiplicity in events at mSUGRA point 5. Distributions are shown for **(a)** all SUSY production and **(b)** $\tilde{q}_R\tilde{q}_R$, $\tilde{q}_R\tilde{q}_L$ and $\tilde{q}_L\tilde{q}_L$ production.

Figures 5.8a and 5.8b show the jet multiplicity distribution of all SUSY events and for $\tilde{q}_R\tilde{q}_R$, $\tilde{q}_L\tilde{q}_L$ and $\tilde{q}_R\tilde{q}_L$ production. Nearly all right-squarks decay via $\tilde{q}_R \to \tilde{\chi}_1^0 q \to qqqq$ and one might therefore expect a mean multiplicity of 8 jets for $\tilde{q}_R\tilde{q}_R$ production. Gluon radiation by quarks, however, raises the mean multiplicity to 10.5 jets. The three jets from harder $\tilde{\chi}_1^0$s are spatially close together and some merging of jets occurs resulting in a small number of events with fewer than 8 jets (6% for all SUSY production). In $\tilde{q}_R\tilde{q}_R$ events, the $\tilde{\chi}_1^0$s are produced directly in the right-squark decay and have a higher mean transverse momentum than $\tilde{\chi}_1^0$s from longer decay chains (376 GeV for the hard $\tilde{\chi}_1^0$). As a consequence, there is more jet merging and there are more events with less than 8 jets (14%). Gluinos (not shown in figure) mostly decay into a squark and a quark and $\tilde{g}\tilde{g}$ events have a higher mean jet multiplicity of 13.6.

When λ''_{212} is small, there are nearly always two $\tilde{\chi}_1^0$s produced in an event and one can therefore search for two sets of three jets with similar invariant mass. An upper limit on the invariant mass difference of $\delta m_{jjj} = |m_{jjj}^{(a)} - m_{jjj}^{(b)}| < 20$ GeV is used in this analysis. This value was chosen to be approximately twice the width of the matched $\tilde{\chi}_1^0$ mass peak in figure 5.7. This criterion alone does not sufficiently reduce the combinatorial background: In an event with 11 jets there are 9240 ways of choosing two sets of three jets.

One way to reduce the combinatorial background is to only use events with a certain number of jets. The lower bound in this analysis, $n_{jet}^{(min)}$, is 8: the minimum number of quarks produced in a $\tilde{q}_R\tilde{q}_L$, $\tilde{q}_L\tilde{q}_L$ or $\tilde{q}_R\tilde{q}_R$ event. The upper limit, $n_{jet}^{(max)}$, should be high enough to allow some gluon radiation but low enough to keep the combinatorial background small. It is studied in more detail later in this section.

To further restrict the number of jet combinations considered, cuts are placed on the

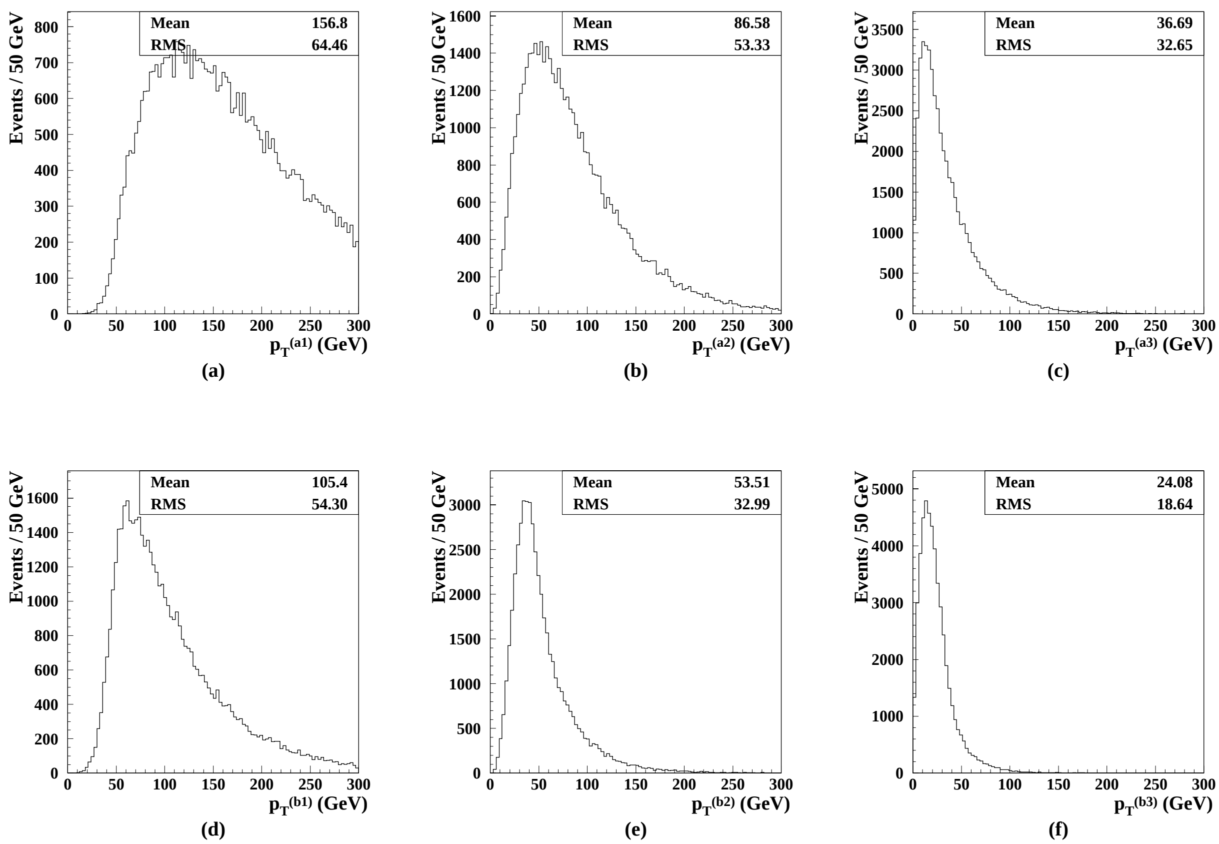

Figure 5.9: Histograms **(a)**, **(b)** and **(c)** show the transverse momenta of the hardest, middle and softest quarks respectively from the hard $\tilde{\chi}_1^0$ decay. Histograms **(d-f)** show the same but for the soft $\tilde{\chi}_1^0$. The transverse momenta were measured at the generator level.

jet kinematics. Figure 5.9 shows the transverse momenta of the HERWIG generated quarks from the hard ($p_T^{(a1)}, p_T^{(a2)}, p_T^{(a3)}$) and the soft ($p_T^{(b1)}, p_T^{(b2)}, p_T^{(b3)}$) $\tilde{\chi}_1^0$. The softest jet of the soft $\tilde{\chi}_1^0$ has a mean transverse momentum of only 24 GeV and so it is necessary to consider both high and low energy jets. The following transverse momentum cuts are used in this analysis (all p_T in GeV):

- $100 < p_T^{(a1)}$; $17.5 < p_T^{(a2)} < 300$; $15.0 < p_T^{(a3)} < 150$
- $17.5 < p_T^{(b1)} < 300$; $17.5 < p_T^{(b2)} < 150$; $15.0 < p_T^{(b3)} < 75$

Candidate sets of jets from the $\tilde{\chi}_1^0$ decay can also be identified by their spatial separation. Figure 5.10 shows, for both $\tilde{\chi}_1^0$s, the angle between the hardest and next hardest quarks (ΔR_{12}) and between the combined momentum vector of the two hardest quarks and the softest quark (ΔR_{12-3}). The following cuts were chosen based on figure 5.10:

- $\Delta R_{12}^{(a)} < 1.3$; $\Delta R_{12-3}^{(a)} < 1.3$
- $\Delta R_{12}^{(b)} < 2.0$

When applying kinematic cuts similar to the above, it is important to ensure that the cuts themselves are not defining the sought mass peak. It is shown later that the mass distribution of background events passing these cuts is significantly wider than the $\tilde{\chi}_1^0$ mass peak.

A hard quark is produced in the decay of a $\tilde{q}_R$, $\tilde{q}_L$ or $\tilde{g}$. In sparton-sparton events, two such hard quarks ($q^{(h1)}$, $q^{(h2)}$) are produced. When measured at the generator level, approximately 75% of such events have $p_T^{(h1)} > 200$ GeV and $p_T^{(h2)} > 100$ GeV. Over 80% of the hard quarks are within $|\eta| < 2$. By requiring that two jets in an event satisfy these cuts, the number of remaining jets from which the $\tilde{\chi}_1^0$s can be reconstructed is reduced, thus reducing the combinatorial background.

Using only cuts on the jet kinematics and jet multiplicity, a mass peak can be seen above the background from wrong combinations of jets. Figure 5.11a shows the mass peak obtained after three years of low luminosity running. The SUSY data sample used to obtain this plot was defined in section 5.6.3.

For each combination of jets passing the kinematic cuts, the reconstructed masses of both the hard and the soft $\tilde{\chi}_1^0$s are included in figure 5.11a. If two or more combinations of jets from one event pass the cuts, the masses from each combination are plotted with unity weight. This method is adopted because there is no way of choosing the best combination. One might, for example, select the jet combination with smallest δm_{jjj}. This variable, however, has a maximum value of 20 GeV which is about the precision of a measurement of δm_{jjj} given that the mass peak width due to detector resolution is 10 GeV (see figure 5.7).

In events with more than one combination passing the cuts, two combinations of jets often differ only in the choice of jets for one of the two $\tilde{\chi}_1^0$s. For example, the jets identified as being from the hard $\tilde{\chi}_1^0$ may be the same in both combinations with the soft $\tilde{\chi}_1^0$ jets being different. In this case, the hard $\tilde{\chi}_1^0$ mass would be included in the

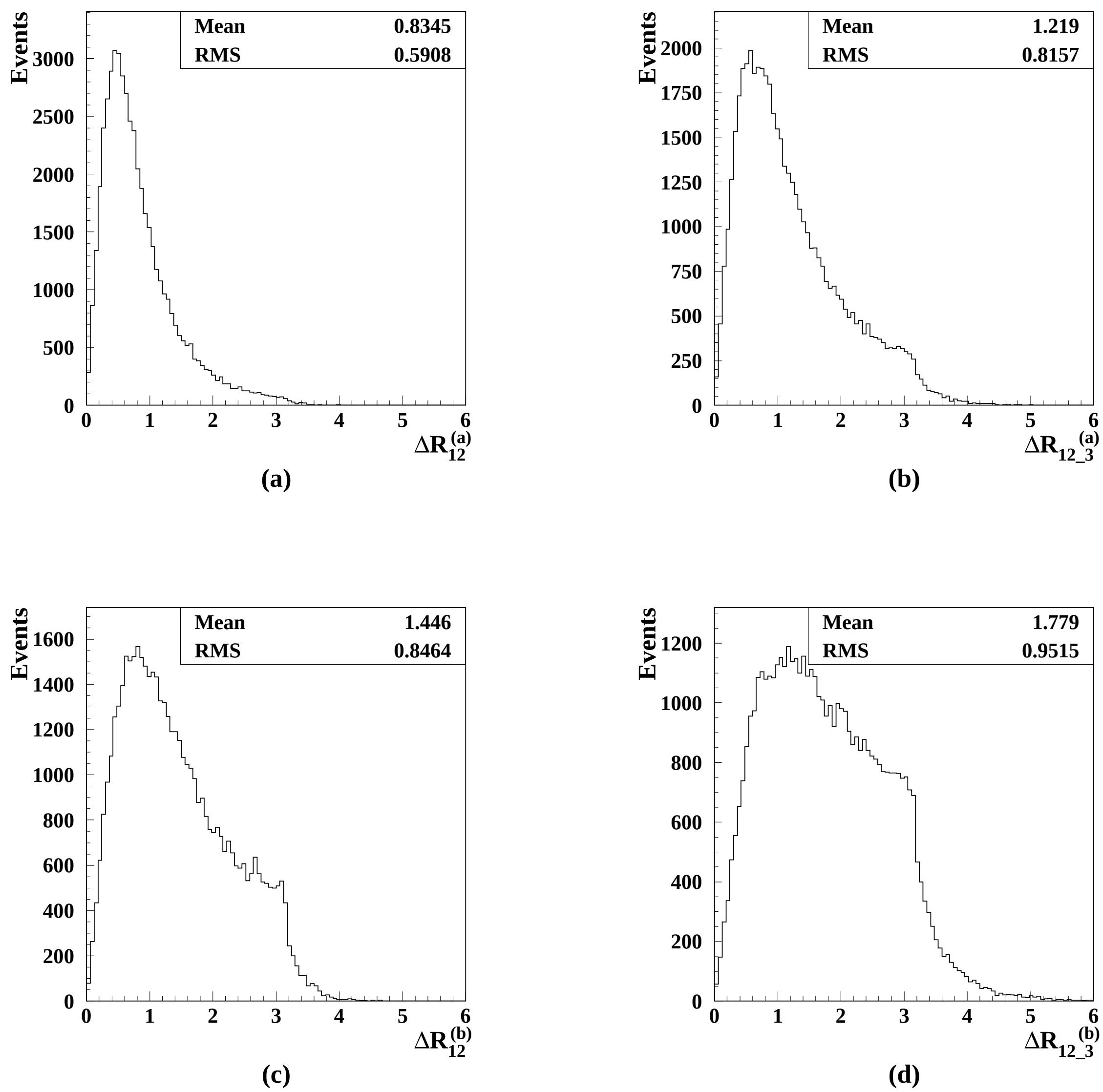

Figure 5.10: The distribution of the separation in (η, ϕ) of: **(a)** the two hardest quarks from the hard $\tilde{\chi}_1^0$ decay; **(b)** The combined momenta of the two hardest quarks and the softest quark from the hard $\tilde{\chi}_1^0$ decay. Histograms **(c)** and **(d)** show the same distributions for the soft $\tilde{\chi}_1^0$ quarks. The separation in ϕ of two quarks is taken to be the smallest of the two possible angles. This results in the observed discontinuities in the histograms at around $dr = \pi$.

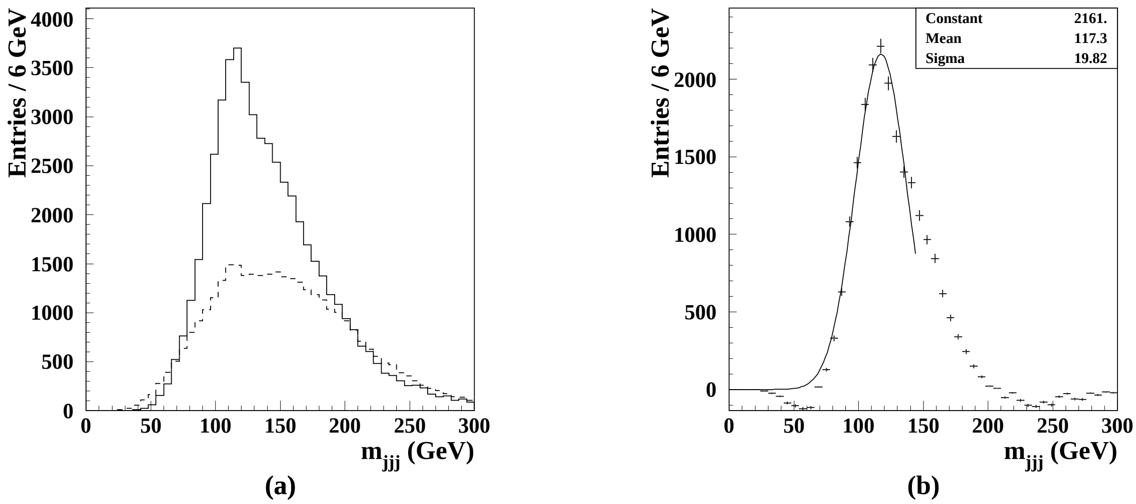

Figure 5.11: **(a)** The solid histogram shows the invariant mass distribution of the three-jet combinations passing the jet cuts described in the text ($n_{jet}^{(max)} = 10$). The dashed histogram shows the background distribution generated from the same data set of 700000 SUSY events (three years of low luminosity running). **(b)** shows the difference between the two histograms in **(a)**.

histogram only once. The two soft $\tilde{\chi}_1^0$ masses would, however, be included with unity weight.

There is a broad combinatorial background beneath the $\tilde{\chi}_1^0$ mass peak, the shape of which is defined by the kinematic cuts and not by a physical process. A distribution of the same shape can therefore be generated from the same data as the $\tilde{\chi}_1^0$ peak by selecting 3-jet combinations that are not from a $\tilde{\chi}_1^0$ decay. It was found that the invariant mass distribution of 3-jet combinations with $20 < |\delta m_{jjj}| < 100$ GeV could be used as an approximation to the background. The shape of the tails of the generated background distribution is very similar to the shape of the $\tilde{\chi}_1^0$ mass peak tails. The generated background distribution, however, has fewer events in the central peak.

A generated and normalised background is superimposed on figure 5.11a. The generated distribution is normalised to the background under the $\tilde{\chi}_1^0$ peak using events in the distribution tails which are defined:

- $(\bar{m}_{jjj} - 3\sigma) < m_{jjj} < (\bar{m}_{jjj} - 2\sigma)$
- $(\bar{m}_{jjj} + 3\sigma) < m_{jjj} < (\bar{m}_{jjj} + 5.5\sigma)$

where $\bar{m}_{jjj}$ and σ are the mean mass and RMS width of the distribution respectively. Figure 5.11b shows the mass peak with the background subtracted. There is still a shoulder on the high mass tail of the distribution. This shoulder can be reduced with further cuts.

Lepton cuts

A pair of OSSF leptons are produced in the decay chain studied in this analysis (figure 5.6a). Requiring that these leptons are observed significantly reduces the number of reconstructed $\tilde{\chi}_1^0$s but leads to an improved mass peak. In any case, the leptons must be identified to find the slepton and $\tilde{\chi}_2^0$ masses and will be seen to be essential in reducing the SM background (section 5.6.5).

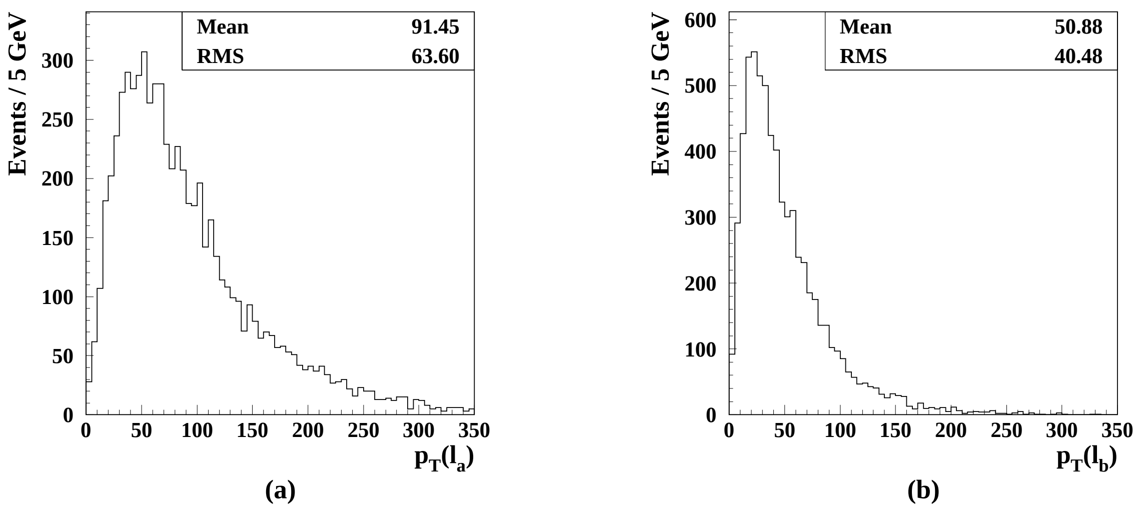

Figure 5.12: The transverse momentum distribution, measured at the generator level, of the lepton from: **(a)** the $\tilde{\chi}_2^0$ decay in the left-squark decay chain; **(b)** the right-slepton decay in the left-squark decay chain.

Figure 5.12 shows the transverse momenta of HERWIG generated leptons ($e^{\pm}$ or $\mu^{\pm}$) from the $\tilde{\chi}_2^0$ and right-slepton decays in the left-squark decay chain. These leptons are labelled l_a and l_b respectively for convenience of reference. Approximately 95% and 85% of the leptons in figures 5.12a and 5.12b respectively have a transverse momentum greater than 15 GeV.

Events passing the jet cuts ($n_{jet}^{(max)} = 10$) and containing two OSSF leptons with $p_T > 15$ GeV were selected. The distribution of the invariant mass of the two leptons, m_{ll}, is plotted in figure 5.13. To determine the sample purity, the leptons were matched spatially to the HERWIG generated particles. 26% of lepton pairs found by ATLFAST had at least one lepton not from the decay chain, $\tilde{\chi}_2^0 \to \tilde{l}_R l \to ll\tilde{\chi}_1^0$. This background is shown as the hatched component of the histogram. Using dedicated cuts, the position of the sharp upper edge was measured in [22] to be at $109 \pm 0.3(\text{stat}) \pm 0.11(\text{syst})$ GeV. In this analysis, a requirement of exactly two OSSF leptons with $p_T > 15$ GeV and with $m_{ll} < 109$ GeV is added to the previously described jet cuts.

Figure 5.14 shows the $\tilde{\chi}_1^0$ mass distributions obtained with lepton and jet cuts. In figure 5.14a the distribution before background subtraction is shown for an upper limit of 10 jets. The mass peaks with background subtracted are shown in figures 5.14b-d for

$n_{jet}^{(max)} = 9$, 10 and 11 respectively. Table 5.7 summarises the reconstruction efficiency, bias and mass precision for the three values of $n_{jet}^{(max)}$.

The optimal upper limit on the number of jets is $n_{jet}^{(max)} = 10$. For $n_{jet}^{(max)} = 11$ the reconstruction efficiency and mass precision are better but there is a small shoulder on the mass peak between 130 GeV and 150 GeV which is not present for lower values of $n_{jet}^{(max)}$. This shoulder results in a less negative bias for $n_{jet}^{(max)} = 11$ than for $n_{jet}^{(max)} = 10$. Using spatial matching of $\tilde{\chi}_1^0$s, it was shown, in section 5.6.2, that the expected bias is -10 GeV (see figure 5.7). The reconstruction efficiencies ϵ_1 and ϵ_2 are 1.5 and 1.8 times larger for $n_{jet}^{(max)} = 11$ than for $n_{jet}^{(max)} = 10$. The number of events in the $\tilde{\chi}_1^0$ mass peak increases by a factor of 3 when $n_{jet}^{(max)}$ is increased from 10 to 11. The ratio of good to background entries is therefore better in the peak with $n_{jet}^{(max)} = 10$.

A small peak is seen on the upper tail of the mass distributions in each of the plots in figure 5.14. The position of this peak approximately coincides with the mass of the lighter right-sleptons in the mSUGRA point 5 scenario. It was concluded in [22] that the slepton mass is found when the lepton from a slepton decay is not isolated but inside one of the three $\tilde{\chi}_1^0$ jets. Since the cone used to define a cluster is narrow ($\Delta R = 0.4$) the invariant mass of the three $\tilde{\chi}_1^0$ jets would in fact be approximately the invariant mass of the jets and the lepton. To produce figure 5.14, a cut of exactly 2 isolated leptons was applied to the data. If the lepton from the slepton decay is within a jet, a lepton from another source is needed to give a total of two isolated leptons.

To test the hypothesis that the secondary peak is due to a reconstructed slepton mass, the two leptons identified by ATLFAST were spatially matched to the HERWIG generated leptons from the $\tilde{\chi}_2^0$ and slepton decays. When the $\tilde{\chi}_1^0$ mass distribution was plotted using only events in which there was a good match between the ATLFAST and HERWIG leptons, the secondary peak was still observed. It was also noted that in events with matched leptons, only one slepton was generated by HERWIG. This evidence suggests that the hypothesis is incorrect and that the peak has another origin.

The number of events in the secondary peak is much smaller than the number of events in the signal and background peaks beneath it. It was, therefore, not possible to identify the source of the secondary peak.

b-tagging cuts

No b-quarks are produced in the $\tilde{\chi}_1^0$ decay if the only non-zero RPV coupling is λ''_{212}. Some wrong combinations of jets can therefore be eliminated by using b-jet tagging. In practice, for a high b-tagging efficiency there is a finite chance of mis-tagging non b-jets (table 5.3). The mis-tagging probability is highest for c-jets, two of which are produced in most events when $\lambda''_{212} = 0.005$. For a b-tagging efficiency of 64%, there is a 25% probability of mis-tagging a c-jet and therefore a 50% chance of rejecting a correct combination of 6 jets from 2 $\tilde{\chi}_1^0$s. For lower b-tagging efficiencies, an improved c-jet rejection can, however, be obtained.

To investigate the usefulness of b-tagging, a b-jet veto was added to the lepton and jet cuts. Any combination of three jets containing a b-tagged jet was rejected. Table 5.8 lists the bias, efficiency and precision of the $\tilde{\chi}_1^0$ mass reconstruction for three different

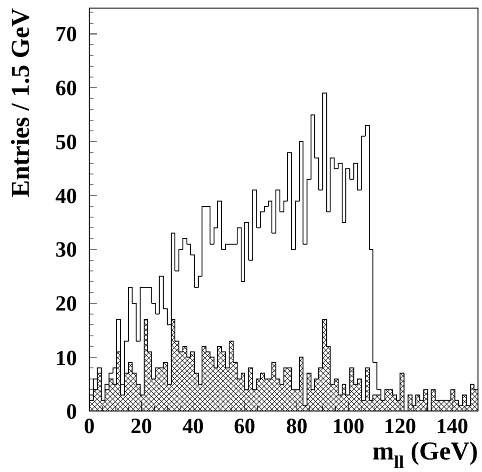

Figure 5.13: The invariant mass distribution of the 2 leptons found by applying the jet cuts described in the text and requiring two leptons with $p_T > 15$ GeV. The shaded section of the histogram shows the m_{ll} distribution of lepton pairs not from the decay $\tilde{\chi}_2^0 \rightarrow \tilde{l}_R l \rightarrow ll\ \tilde{\chi}_1^0$.

$n_{jet}^{(max)}$	Reconstruction efficiency		Bias	Mass precision
	ϵ_1(%)	ϵ_2 (%)	(GeV)	(GeV)
9	0.4	0.1	-3.0	0.87
10	1.1	0.4	-5.1	0.43
11	2.0	0.6	-5.0	0.26

Table 5.7: The efficiency, bias and precision of the $\tilde{\chi}_1^0$ reconstruction for the lepton and jet cuts. In three years, 27000 SUSY events in which exactly one $\tilde{\chi}_2^0$ decays via a slepton are expected. ϵ_1 is the fraction of these events in which at least one reconstructed $\tilde{\chi}_1^0$ was well matched to the generated sparticle. ϵ_2 is the fraction of events with two matched $\tilde{\chi}_1^0$s.

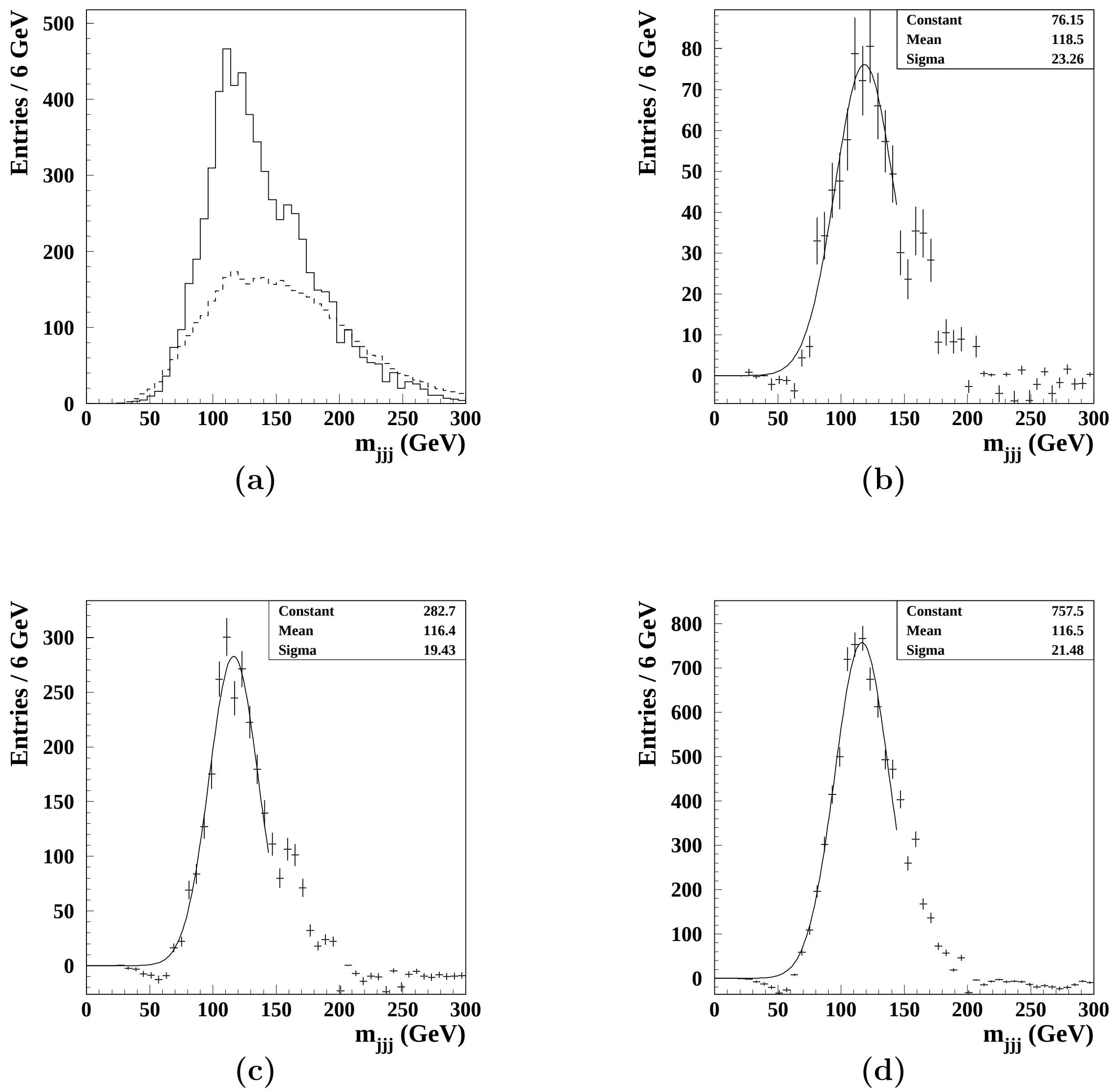

Figure 5.14: **(a)** The invariant mass of three-jet combinations passing the lepton and jet cuts (solid histogram) and generated background distribution (dashed histogram) for $n_{jet}^{(max)} = 10$. The m_{jjj} distributions with background subtracted are shown for **(b)** $n_{jet}^{(max)} = 9$, **(c)** $n_{jet}^{(max)} = 10$ and **(d)** $n_{jet}^{(max)} = 11$. All histograms were generated from a sample of 700000 SUSY events.

b-tagging efficiency (%)	c-jet rejection factor	Reconstruction efficiency		bias (GeV)	mass precision (GeV)
		ϵ_1(%)	ϵ_2 (%)		
100%	∞	1.08	0.38	-5.3	0.4
33%	22.9	1.04	0.38	-4.2	0.4
64%	4.2	0.67	0.23	-4.6	0.5

Table 5.8: The efficiency, bias and precision of the $\tilde{\chi}_1^0$ mass reconstruction with lepton, jet ($n_{jet}^{(max)} = 10$) and b-tagging cuts for three different b-tagging efficiencies.

b-tagging efficiencies.

A small improvement in the mass peak bias is seen for an unrealistic b-tagging efficiency of 100%. When a realistic b-tagging efficiency is used, however, the reconstruction efficiency is degraded without a significant improvement in the mass precision or the bias of the mass peak. b-tagging is, therefore, not used in this study.

Cuts summary

For convenience, the chosen cuts are listed together (all p_T in GeV):

- Number of jets in an event: $8 \leq n_{jet} \leq 10$
- Kinematic cuts on $\tilde{\chi}_1^0$ jets:
  - $100 < p_T^{(a1)}$; $17.5 < p_T^{(a2)} < 300$; $15.0 < p_T^{(a3)} < 150$
  - $17.5 < p_T^{(b1)} < 300$; $17.5 < p_T^{(b2)} < 150$; $15.0 < p_T^{(b3)} < 75$
  - $\Delta R_{12}^{(a)} < 1.3$; $\Delta R_{12-3}^{(a)} < 1.3$
  - $\Delta R_{12}^{(b)} < 2.0$
- Kinematic cuts on hard jets:
  - $p_T^{(h1)} > 200$; $|\eta^{(h1)}| < 2$
  - $p_T^{(h2)} > 100$; $|\eta^{(h2)}| < 2$
- Lepton cuts
  - $p_T^{(l^a)} > 15$; $p_T^{(l^b)} > 15$
  - m_{ll} <109 GeV

In this chapter, these cuts will be referred to as follows:

- Jet cuts = cuts on jet multiplicity + cuts on $\tilde{\chi}_1^0$ jets + cuts on hard jets
- Dilepton cuts = jet cuts + lepton cuts

It is shown in later sections that the dilepton cuts alone are sufficient to extract the $\tilde{\chi}_1^0$, slepton and $\tilde{\chi}_2^0$ masses from SUSY events.

The $\tilde{\chi}_1^0$ mass peak so far obtained has a central mass of 116.4 GeV which is significantly higher than the centre of the matched mass peak (111 GeV). The distribution from the dilepton cuts is also twice as wide as the matched peak. Later in this chapter it is shown that a $\tilde{\chi}_1^0$ mass consistent with the matched mass distribution can be obtained. This suggests that there is a significant number of background entries in the mass peak from the dilepton cuts and that this background biases the peak to a higher mass.

In some mSUGRA models, the lightest right-sleptons are more massive than the $\tilde{\chi}_2^0$ and the decay chain exploited by the dilepton cuts is not present. In such a scenario, it would be important to better understand the bias of the mass peak obtained with the jet cuts alone.

5.6.5 SM backgrounds

The dilepton cuts used to extract a $\tilde{\chi}_1^0$ mass from the SUSY background are exacting. The SM production processes listed in table 5.9 were used to investigate whether further cuts are needed to suppress SM backgrounds.

The cross section of QCD processes are large and it would be impossible to generate a useful fraction of the expected number of QCD events. The QCD cross section, however, is dominated by soft events. If it can be shown that such events would not pass some set of selection cuts, then only energetic QCD events need to be considered. For this reason, the QCD cross section is listed for ranges of $p_T^{(2-2)}$, the transverse momentum of both out-going partons of the hard process. Other SM background processes have been similarly divided.

Table 5.10 lists the number of SM events generated and passing three different sets of cuts:

- Jet cuts (defined in section 5.6.4)
- One-lepton cuts: Jet cuts + at least one lepton with $p_T > 15$ GeV
- Dilepton cuts (section 5.6.4)

Only 12 of the 13×10^6 generated QCD events pass the dilepton cuts. From just 12 events it is impossible to draw conclusions about which $p_T^{(2-2)}$ ranges should be regarded as a source of background events. Without more information, QCD events with $10 < p_T^{(2-2)} < 100$ cannot be disregarded. And for the generated sample of 2.5×10^6 events, this QCD $p_T^{(2-2)}$ range has a 90% upper confidence limit of 1.5×10^8 events.

Fortunately, the rejection power of the dilepton cuts at different $p_T^{(2-2)}$ can be inferred from the looser one-lepton and jet cuts. The effectiveness of a set of cuts against a certain process can be measured by the fractional cross section which is defined as $\sigma_f = \sigma n/N$ where σ is the process cross section, N is the number of events generated and n is the number of events passing the cuts. The rate at which events would pass the cuts is the product of σ_f and the LHC luminosity. Figure 5.15 shows σ_f plotted against $p_T^{(2-2)}$ for QCD events. The probability of a QCD event passing the jet cuts is seen to fall sharply below $p_T^{(2-2)} = 200$ GeV. It is inferred that a similar fall occurs for the 1 lepton and 2 lepton cuts and that the contribution from QCD events with $p_T^{(2-2)} < 200$ GeV is insignificant.

The last column of table 5.10 lists the 90% upper confidence limit on the number of events passing the 2 lepton cuts. A total of 2058 events is found for the processes considered. In the $\tilde{\chi}_1^0$ mass peak, there are 6404 entries before background subtraction (figure 5.14a). The combined distribution from SM and SUSY processes would, therefore, not be dominated by SM backgrounds and, by using a background subtraction, it should still be possible to extract a $\tilde{\chi}_1^0$ mass peak. In section 5.6.6, it will be shown that nearly all combinatorial SUSY background can be removed from the $\tilde{\chi}_1^0$ mass peak using the 2 leptons produced in the $\tilde{\chi}_2^0$ decay chain. This method is likely to also be effective at removing any SM background.

Process	$p_T^{(min)}$ (GeV)	$p_T^{(max)}$ (GeV)	Cross section (pb)	Events in 3 years
QCD	10	100	4.95×10^9	1.6×10^{14}
QCD	100	200	1.26×10^6	4.0×10^{10}
QCD	200	300	5.87×10^4	1.9×10^9
QCD	300	400	8045	2.6×10^8
QCD	400	500	1766	5.7×10^7
QCD	500	600	507.1	1.6×10^7
QCD	600	700	173.6	5.6×10^6
QCD	700	10^8	122.7	3.9×10^6
$t\bar{t}$	10	100	258.3	8.3×10^6
$t\bar{t}$	100	10^8	321.3	10.3×10^6
Z+jets	10	100	4448	1.4×10^8
Z+jets	100	10^8	134.5	4.3×10^6
W+jets	10	100	5.67×10^4	1.8×10^9
W+jets	100	10^8	1411	45.2×10^6
SUSY	10	10^8	21.89	700000

Table 5.9: The cross sections of potential SM backgrounds. Each process is divided into ranges of $p_T^{(2-2)}$, the transverse momentum of each of the two out-going partons from the hard process.

Process ($p_T^{(min)}$, $p_T^{(max)}$)	Events generated	Events passing cuts			Dilepton cut 90% upper CL (in 3 years)
		Jets	1 lepton	Dilepton	
QCD (10,100)	2.5×10^6	0	0	0	-
QCD (100,200)	2.5×10^6	183	0	0	-
QCD (200,300)	4.0×10^6	31×10^3	54	0	1093
QCD (300,400)	2.0×10^6	121×10^3	194	0	299.0
QCD (400,500)	0.5×10^6	63×10^3	187	0	262.2
QCD (500,600)	0.5×10^6	104×10^3	377	0	73.6
QCD (600,700)	0.5×10^6	112×10^3	541	4	89.5
QCD (700,10^8)	0.5×10^6	162×10^3	1176	8	101.0
$t\bar{t}$ (10,100)	2.5×10^6	303	11	0	7.6
$t\bar{t}$ (100,10^8)	7.9×10^6	186×10^3	8.8×10^3	15	27.8
Z+jets (10,100)	0.5×10^6	0	0	0	-
Z+jets (100,10^8)	1.0×10^6	571	0	0	-
W+jets (10,100)	0.5×10^6	0	0	0	-
W+jets (100,10^8)	1.0×10^6	643	5	0	104
				Total	2058

Table 5.10: The number of SM events generated and passing the three sets of SUSY cuts described in the text. The right-most column gives the 90% upper confidence limit on the number of events passing the dilepton cuts.

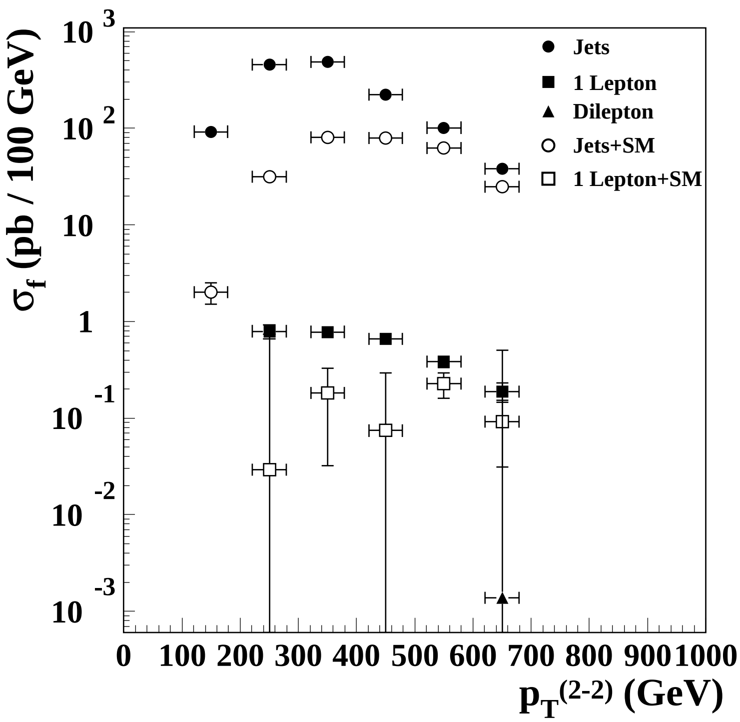

Figure 5.15: The fractional QCD cross section, σ_f, plotted against $p_T^{(2-2)}$ for various SM and SUSY cuts.

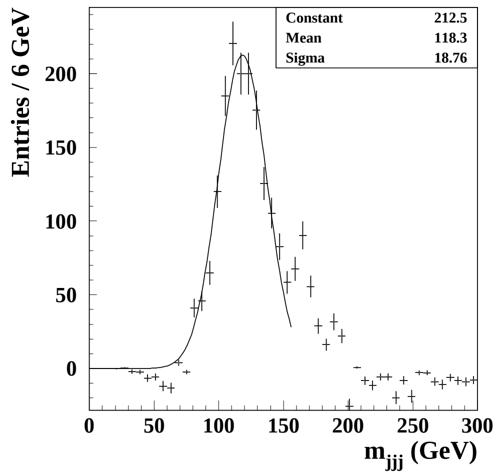

Figure 5.16: The $\tilde{\chi}_1^0$ mass distribution with BG subtracted for three-jet combinations passing the dilepton and SM cuts (700000 SUSY events generated).

It is possible that the SM background has been underestimated. In [28], particle level simulations were shown to give lower QCD rates than full Monte Carlo simulations. If necessary, additional cuts can be used to further reduce the SM background. For example, the following cuts are used in [22] to obtain an implicit SUSY signature in RPV mSUGRA models:

- Thrust cut: $T = \max_{\vec{n}} \frac{\sum_i |\vec{p_i}.\vec{n}|}{\sum_i |\vec{p_i}|} < 0.9$
- Sphericity cut: $S = \frac{3}{2} \min_{\vec{n}} \frac{\sum_i |\vec{p_i}.\vec{n}|}{\sum_i |\vec{p_i}|} > 0.1$
- Transverse energy cut: $m_T^{(cent)} = \sum_{|\eta|<2} p_T^{(jet)} + \sum_{|\eta|<2} p_T^{(lepton)} > 1000$ GeV

The thrust and sphericity are maximised and minimised respectively by the choice of the vector $\vec{n}$. The sums are over all jet three-momenta. Both T and S measure the spherical symmetry of an event. For a pencil-like event, with partons produced back to back in narrow cones, $T = 1$ and $S = 0$. In an isotropic event $T = \frac{1}{2}$. The sums in $m_T^{(cent)}$ are over all jets and leptons with $|\eta| < 2$. In this chapter, these three cuts are referred to as the SM cuts.

In figure 5.15, σ_f is plotted for the SM cuts added to the jet and 1 lepton cuts. The SM background is reduced, especially at lower values of $p_T^{(2-2)}$. Figure 5.16 shows the $\tilde{\chi}_1^0$ mass peak with the SUSY and SM cuts applied to the SUSY data-set. The efficiency of reconstructing at least one well matched $\tilde{\chi}_1^0$, $\epsilon_1 = 0.84\%$. The reconstruction efficiency for two well matched $\tilde{\chi}_1^0$s is 0.27%. Although the $\tilde{\chi}_1^0$ reconstruction efficiency is lower than for just SUSY cuts, a $\tilde{\chi}_1^0$ mass peak can still be found.

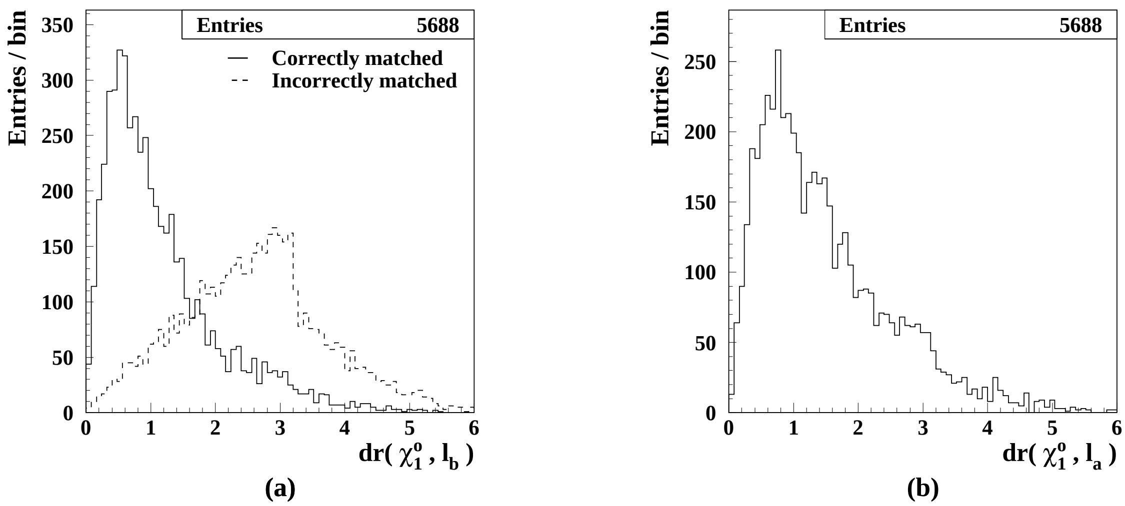

Figure 5.17: **(a)** The solid histogram shows the separation in (η,ϕ) of a $\tilde{\chi}_1^0$ and lepton from a slepton decay. The dashed histogram shows the separation between the same lepton and the other $\tilde{\chi}_1^0$ in the event. **(b)** The separation in (η,ϕ) of the lepton produced in the decay $\tilde{\chi}_2^0 \to \tilde{l}l$ and the $\tilde{\chi}_1^0$ from the slepton decay.

5.6.6 Measuring the slepton and $\tilde{\chi}_2^0$ masses

Nearly all right-selectrons and right-smuons decay into a $\tilde{\chi}_1^0$ and a lepton. The slepton mass can be measured by finding the invariant mass of these two particles.

The dilepton cuts, defined in section 5.6.4, require a pair of OSSF leptons with $m_{ll}^{(max)} < 109$ GeV. These cuts are intended to select leptons from the $\tilde{\chi}_2^0$ and slepton decays in the left-squark decay chain. Spatial matching was used to assess the purity of events passing the cuts. In 74% of events, the 2 leptons found by ATLFAST were from the $\tilde{\chi}_2^0$ and slepton decays.

In section 5.6.4, a $\tilde{\chi}_1^0$ mass peak was found with width 19.4 GeV and centred at 116.4 GeV. A statistical subtraction was used to remove a broad background beneath the $\tilde{\chi}_1^0$ mass peak. Three-jet combinations passing the dilepton cuts and with m_{jjj} within 2 standard deviations (38.8 GeV) of the mass peak centre are used to find the slepton mass. The fact that a statistical background subtraction was used to obtain the $\tilde{\chi}_1^0$ mass peak indicates that a large fraction of the 3-jet combinations in this sample are from backgrounds.

For now, it is assumed that an accurate jet energy scale correction for high jet multiplicity is used. The 4-momenta of jets from $\tilde{\chi}_1^0$ decays are multiplied by a correction factor, $c_j = \frac{m_{\tilde{\chi}_1^0}}{m_{jjj}}$ where $m_{\tilde{\chi}_1^0}$ is the true $\tilde{\chi}_1^0$ mass and m_{jjj} is the invariant mass of the three jets before calibration. The jet energy scale correction will be considered in detail in section 5.6.9.

There are two leptons and two $\tilde{\chi}_1^0$s in each event selected by the dilepton cuts. The spatial separation of particles was used to identify the particles from the slepton

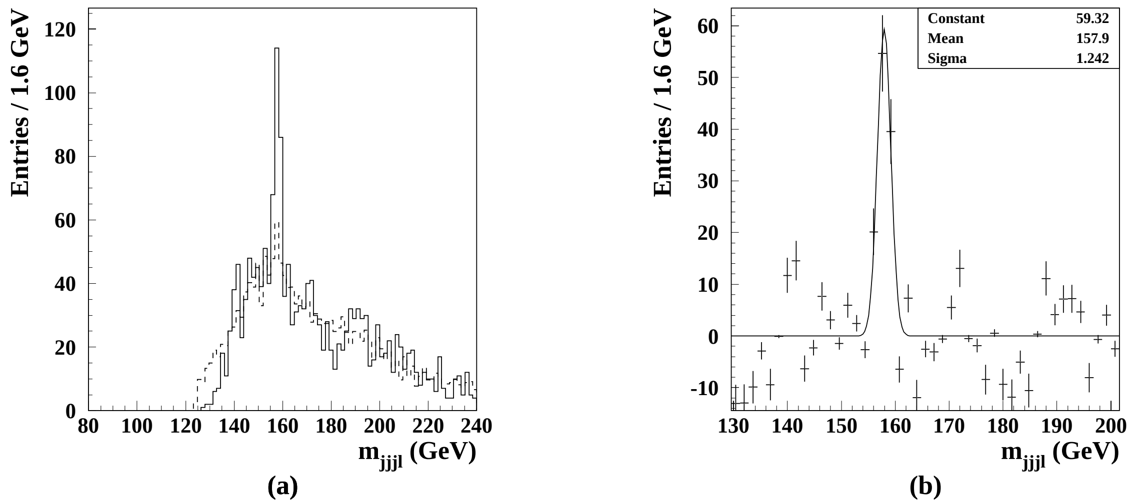

Figure 5.18: **(a)** The solid histogram shows the invariant mass of the $\tilde{\chi}_1^0$ and l_b found using the algorithm described in the text. A sharp peak at approximately 160 GeV is clearly visible. A generated background histogram is also shown (dashed histogram). **(b)** The m_{jjjl} distribution with background subtracted.

decay. Figure 5.17a shows $dr(\tilde{\chi}_1^0, l_b)$, the angular separation between the $\tilde{\chi}_1^0$ from the slepton decay and the lepton, l_b, from the slepton decay measured at the generator level. Figure 5.17b shows $dr(\tilde{\chi}_1^0, l_a)$, the separation between the $\tilde{\chi}_1^0$ from the slepton decay and the lepton, l_a, from the $\tilde{\chi}_2^0$ decay. 65% of events have $dr(\tilde{\chi}_1^0,l_b) < dr(\tilde{\chi}_1^0,l_a)$. Also superimposed on figure 5.17a is the distribution of the separation between l_b and the $\tilde{\chi}_1^0$ from the other sparton decay chain of the event. On average, the $\tilde{\chi}_1^0$ and l_b from the same slepton are closer together than wrong combinations. In this analysis, the invariant mass of the lepton-$\tilde{\chi}_1^0$ pair with the smallest angular separation is used as a measure of the slepton mass.

Figure 5.18a shows the distribution obtained for m_{jjjl}, the invariant mass of the three jets and lepton. A narrow peak is seen at approximately the true slepton mass (157.2 GeV). There is large background under the slepton peak which has several sources:

- Background three-jet combinations from the $\tilde{\chi}_1^0$ mass peak
- Leptons not from the $\tilde{\chi}_2^0$ decay chain
- Wrong combinations of the $\tilde{\chi}_1^0$ and lepton

A background distribution to m_{jjjl} was generated by applying the above described slepton mass algorithm to the three-jet combinations used to generate the m_{jjj} background. The generated slepton mass background is superimposed on figure 5.18a. It has been normalised to the observed background using histogram bins with $m_{jjjl} > 175$ GeV.

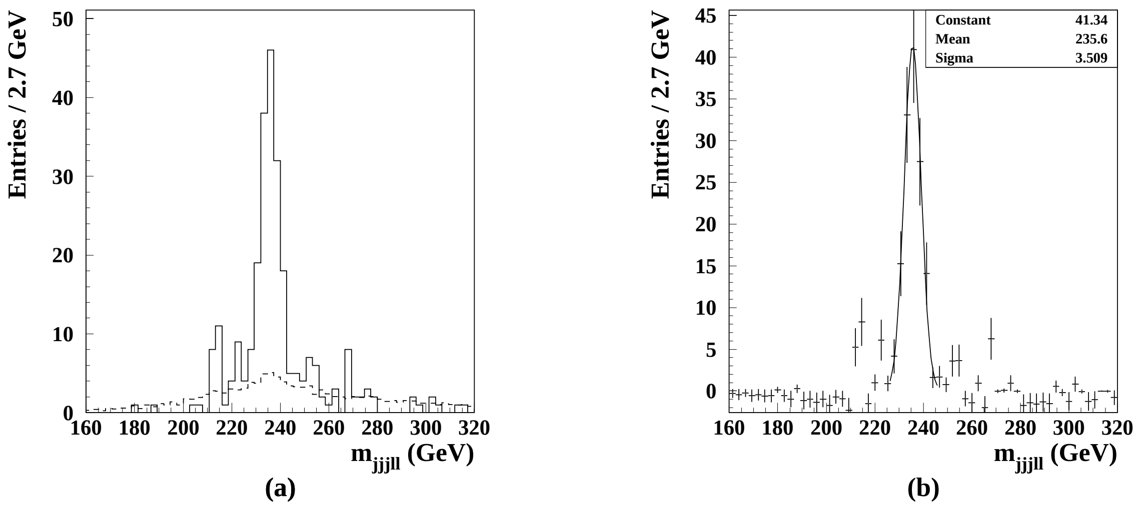

Figure 5.19: **(a)** The m_{jjjll} distribution obtained using the algorithm described in the text. The small background can be generated (dashed histogram). **(b)** The m_{jjjll} distribution with the generated background subtracted.

Figure 5.18b shows the slepton mass peak with the background subtracted. The fitted Gaussian has a mean value of 157.9 ± 0.1 GeV and a width of 1.2 ± 0.1 GeV. A cleaner mass peak is obtained in the next section.

The $\tilde{\chi}_2^0$ mass is the invariant mass of the slepton and the unused lepton. Events with $|m_{jjjl} - 157.9| < 2.4$ GeV were used to obtain the $\tilde{\chi}_2^0$ mass peak shown in figure 5.19a. The small background below the peak can again be generated and subtracted to give the distribution shown in figure 5.19b. The Gaussian fitted to the peak has a mean value of 235.6 ± 0.3 GeV and a width of 3.5 ± 0.2 GeV. The systematic errors of the mass measurement are discussed in section 5.6.9.

5.6.7 Remeasuring the $\tilde{\chi}_1^0$ and slepton masses

By selecting events with a $\tilde{\chi}_2^0$ mass in the peak of figure 5.19b, the background entries in the slepton and $\tilde{\chi}_1^0$ peaks can be almost entirely removed. The $\tilde{\chi}_1^0$ and slepton mass distributions for these events are plotted in figures 5.20a and 5.20b. There are 170 entries in each histogram. The mean $\tilde{\chi}_1^0$ mass agrees, within errors, with the position of the matched mass peak in figure 5.7.

Table 5.11 summarises the masses found for the $\tilde{\chi}_1^0$, slepton and $\tilde{\chi}_2^0$. The two OSSF leptons identified by the cuts can either be electrons or muons. The contributions from both lepton types are shown in the table. Decay chains involving selectrons and smuons are seen to be selected by the cuts in approximately equal proportions. The mass peak centre and width measurements for electron and muon events are equal within errors.

In this analysis, 100% muon and electron identification efficiencies have been assumed. In the actual experiment, an electron efficiency of greater than 90% will be

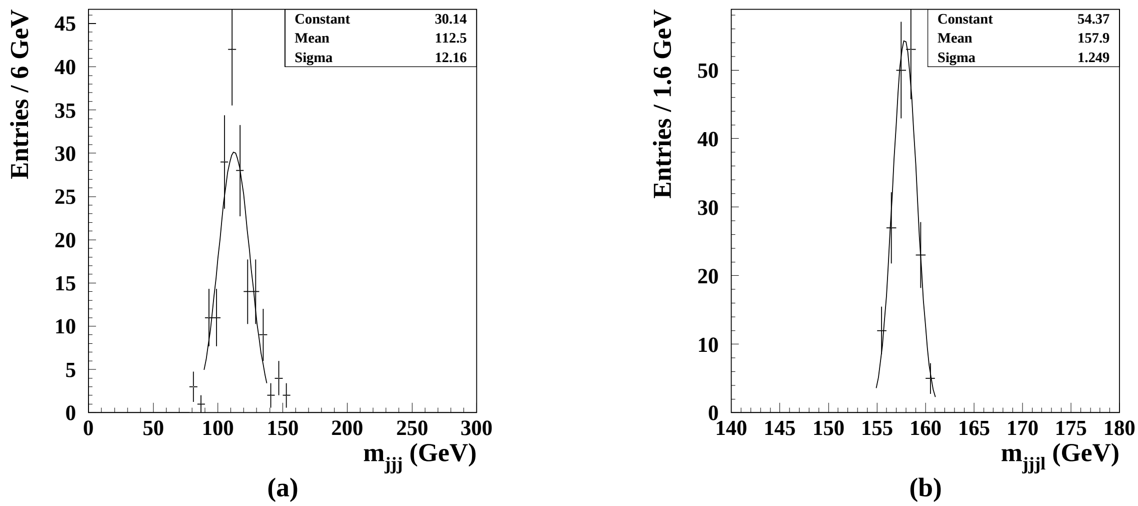

Figure 5.20: **(a)** $\tilde{\chi}_1^0$ and **(b)** slepton mass distributions obtained using events with $|m(\tilde{\chi}_2^0) - 235.6| < 7.0$ GeV

Lepton	Entries	$\tilde{\chi}_1^0$		Slepton		$\tilde{\chi}_2^0$	
		Mean	Width	Mean	Width	Mean	Width
$e^{\pm}$	81	111.0 ± 1.1	8.6 ± 1.6	157.6 ± 0.2	1.2 ± 0.1	236.0 ± 0.6	3.6 ± 0.6
$\mu^{\pm}$	89	114.3 ± 1.5	12.5 ± 1.2	158.2 ± 0.1	1.2 ± 0.1	235.4 ± 0.5	3.8 ± 0.4
Both	170	112.5 ± 1.2	12.2 ± 1.6	157.9 ± 0.1	1.2 ± 0.1	235.6 ± 0.3	3.5 ± 0.2

Table 5.11: A summary of the values found for the $\tilde{\chi}_1^0$, slepton and $\tilde{\chi}_2^0$ masses. The widths listed are the widths of the Gaussian fitted to the centre of the mass distribution. All mean and width values are in GeV. The statistical error on each value is also shown.

achievable for electrons with $p_T > 15$ GeV [17]. The muon reconstruction efficiency is better than 97% for muons with $p_T > 15$ GeV [17]. With these efficiencies one would expect the loss of around 21 of the 170 events passing all cuts.

5.6.8 Loosening the jet multiplicity cut

In sections 5.6.6-5.6.7, the dilepton cuts, defined in section 5.6.4, were used to select the sample of three-jet combinations with which leptons were combined to find the slepton and $\tilde{\chi}_2^0$ masses. The dilepton cuts impose an upper limit on the jet multiplicity of $n_{jet}^{(max)} = 10$. This maximum jet multiplicity was chosen to minimise the background contribution to the $\tilde{\chi}_1^0$ mass peak whilst retaining as many well reconstructed $\tilde{\chi}_1^0$s as possible (page 26). By adding cuts on the $\tilde{\chi}_2^0$ mass to the dilepton cuts, it was shown in section 5.6.7 that nearly all background entries can be eliminated. It is therefore possible to loosen the jet multiplicity cut and obtain clean $\tilde{\chi}_1^0$, slepton and $\tilde{\chi}_2^0$ mass distributions with more entries. Table 5.12 lists the masses obtained for various values of $n_{jet}^{(max)}$. Figure 5.21 shows the $\tilde{\chi}_1^0$, slepton and $\tilde{\chi}_2^0$ mass distributions for $n_{jet}^{(max)} = 12$. The mass peaks for $n_{jet}^{(max)} > 12$ were observed to have significant contributions from backgrounds.

5.6.9 Systematic errors

The uncertainty in the jet energy scale will dominate the systematic errors on the $\tilde{\chi}_1^0$, slepton and $\tilde{\chi}_2^0$ masses. A simple cone algorithm was used in this analysis to identify jets from the $\tilde{\chi}_1^0$ decay. A more sophisticated algorithm would be used in a precision mass measurement. It has nevertheless been demonstrated here that some light sparticle masses can be measured using the cone algorithm. The systematics of these measurements are considered below.

A logical next step in this analysis would be to use a jet clustering algorithm more suited to high multiplicity events. One choice might be the vector cell cluster algorithm which, instead of combining individual jets, finds the invariant mass of all calorimeter cells within a certain region. This algorithm minimises problems from energy sharing between clusters and out-of-cone energy losses. In [29], the cell vector algorithm was used to find the W mass from nearly colinear jets using parton level and full simulations. The results from the two simulations were found to differ significantly. An analysis using the cell vector algorithm is, therefore, best performed using full simulation and is beyond the scope of this study.

$\tilde{\chi}_1^0$ mass systematics

Several effects contribute to the mis-measurement of the mass of a particle reconstructed from 2 or more jets:

- Out-of-cone energy: Not all of a parton's energy is deposited within a cone of half-angle, $\Delta R = 0.4$. The fraction within the cone is p_T and process dependent. Using W+jets events, the ratio $p_T^{(jet)}/p_T^{(partons)}$ was found in [17] to be approximately 0.9

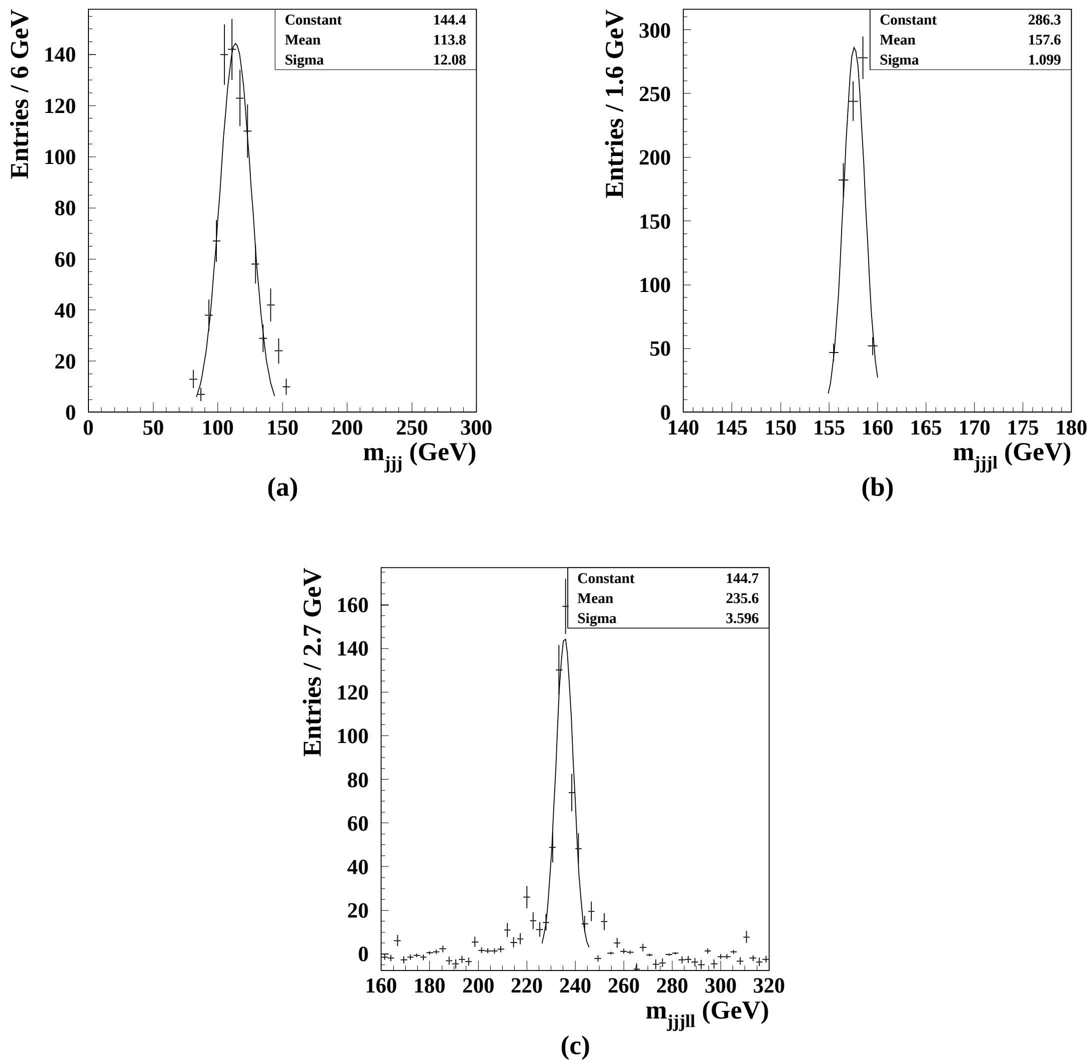

Figure 5.21: **(a)** $\tilde{\chi}_1^0$, **(b)** right-slepton and **(c)** $\tilde{\chi}_2^0$ mass distributions for $n_{jet}^{(max)} = 12$.

$n_{jet}^{(max)}$	Entries	$\tilde{\chi}_1^0$ mass	right-slepton mass	$\tilde{\chi}_2^0$ mass
10	170	112.5 ± 1.2	157.9 ± 0.10	235.6 ± 0.3
11	391	113.6 ± 0.8	157.9 ± 0.05	235.9 ± 0.2
12	803	113.8 ± 0.5	157.6 ± 0.02	235.6 ± 0.2
13	2864	114.3 ± 0.4	157.0 ± 0.1	233.2 ± 0.2

Table 5.12: $\tilde{\chi}_1^0$, right-slepton and $\tilde{\chi}_2^0$ masses found for four upper limits on the jet multiplicity, $n_{jet}^{(max)}$.

for $50 < p_T^{(parton)} < 200$ GeV. This ratio is much closer to unity if a cone with half-angle, $\Delta R = 0.7$ is used.

- Mis-measurement of the angular separation of jets [29].

- Final state radiation (FSR) of partons. [10] considers the reconstruction of the SM Higgs using the decay $H \to b\bar{b}$. The Higgs mass is found with and without FSR simulated. With no FSR or hadronisation, the Higgs mass peak is centred on its nominal mass of 100 GeV. A downward shift of the mass peak of 8 GeV is seen when FSR is turned on. Hadronisation further decreases the mean mass of the peak.

A jet energy correction parameterisation is provided in ATLFAST based on a study of $H \to b\bar{b}$, $H \to u\bar{u}$ and $H \to gg$ reconstruction. The correction is made by multiplying jet 4-momenta by a p_T and jet-flavour dependent number. The correction has not been used in any of the results so far presented in this chapter.

In this study, the accuracy of the ATLFAST jet energy correction is first studied using the hadronic reconstruction of the top-quark. A sample of 2.1×10^5 $t\bar{t}$ events was generated using HERWIG 5.9 with a top mass of 175 GeV. One of the t-quarks was forced to decay leptonically, the other hadronically. Events with four jets, two b-tagged and two from light quarks, were used. The W was reconstructed first by combining the two non-b-jets. Events with a reconstructed W mass within 20 GeV of the true W mass were used to find the top mass. Each b-jet was combined with the W and the invariant mass of the combination with the highest transverse momentum was used as a measure of the top mass.

Figure 5.22 shows the top mass distributions obtained with and without jet energy correction. Before jet energy correction, the fitted Gaussian is centred at 149.9 GeV. When the jet energy correction is applied, the peak overshoots the generated top mass by 5 GeV. By reducing the correction factor by 3.2%, a mass peak with a mean equal, within errors, to the generated top mass was obtained. Each of the three peaks has a low mass tail due to FSR.

In ATLAS, approximately 1500 $t\bar{t}$ events with one top-quark decaying leptonically are expected per day. The reconstruction of the hadronically decaying Ws in these events will be instrumental in understanding jet energy scale systematics [17].

When the modified ATLFAST jet energy reconstruction was applied to the $\tilde{\chi}_1^0$ jets in the 170 events passing all cuts ($n_{jet}^{(max)} = 10$), a $\tilde{\chi}_1^0$ mass peak centred at 129.5 GeV was obtained. The true $\tilde{\chi}_1^0$ mass is 121.5 GeV. Clearly the correction used to find the top mass is not directly applicable. Several possible sources of the discrepancy were investigated. The following are discussed in more detail below: different process kinematics, a different jet multiplicity in events and final state radiation.

The kinematics of the top-quark and $\tilde{\chi}_1^0$ decays are significantly different. The average separation of the two hardest jets in the $\tilde{\chi}_1^0$ decay was found to be approximately $\Delta R = 0.8$. In the $t\bar{t}$ study, the two hardest jets had an average separation of $\Delta R = 1.4$. If the three $\tilde{\chi}_1^0$ jets are nearly touching, one might expect out-of-cone energy losses to be reduced. Geometric arguments can be used to show that one third less energy would

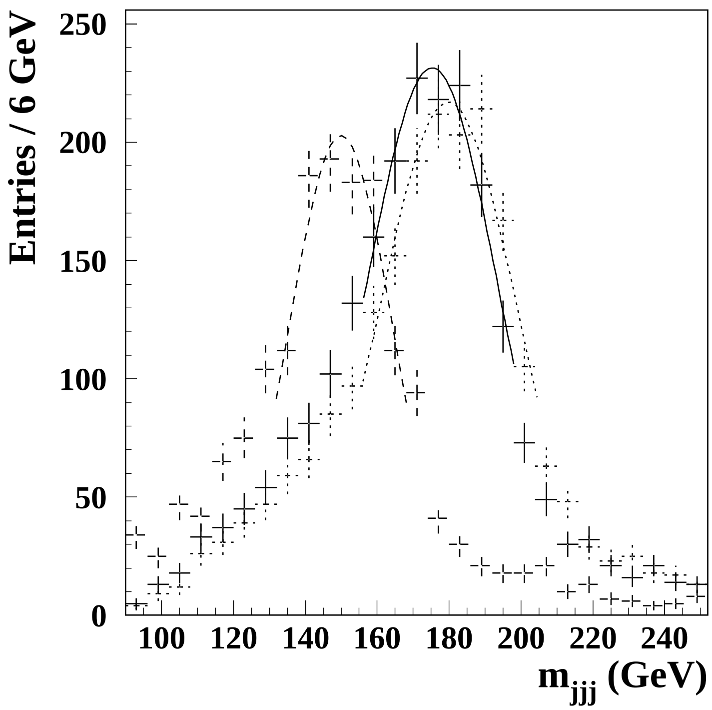

Figure 5.22: The reconstructed top mass for: no energy correction (dashed histogram, $m_t = 149.9 \pm 0.7$ GeV); the standard ATLFAST correction (dotted histogram, $m_t = 179.8 \pm 0.8$ GeV) and a modified ATLFAST correction (solid histogram, $m_t = 175.3 \pm 0.9$ GeV). The result are for 2.1×10^5 $t\bar{t}$ events generated with HERWIG 5.9 with the top mass set to 175 GeV.

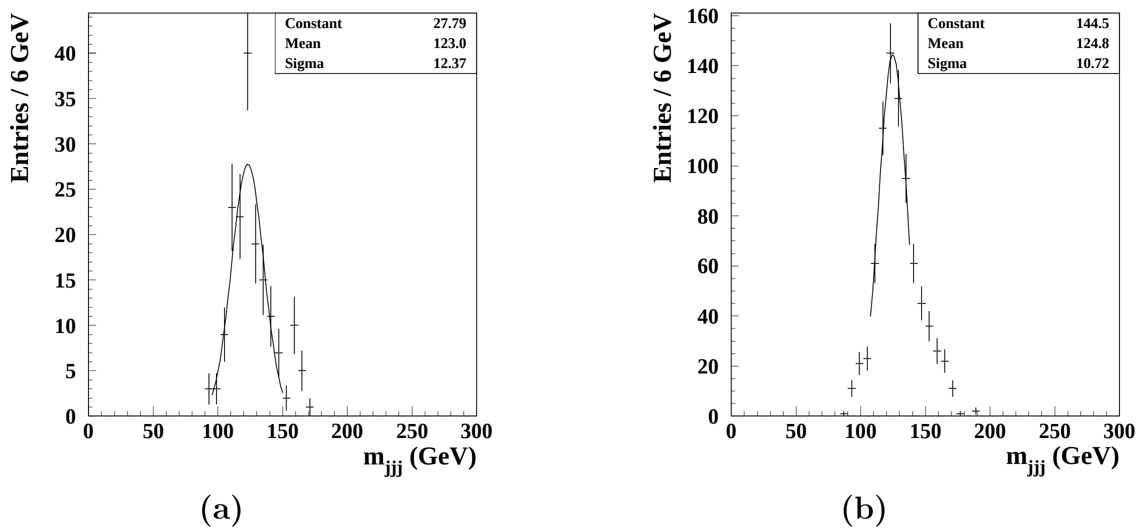

Figure 5.23: The $\tilde{\chi}_1^0$ mass distribution obtained using a modified ATLFAST jet calibration (see text for details) for **(a)** $n_{jet}^{(max)} = 10$ and **(b)** $n_{jet}^{(max)} = 12$.

be lost from three touching cones than from three isolated jets. Also, in [29] the mismeasurement of the angular separation of jets was found to be significant for nearly colinear jets. In this study, however, no correlation was seen between the minimum jet separation and the reconstructed $\tilde{\chi}_1^0$ mass.

Another difference between the $t\bar{t}$ and SUSY events is a higher jet multiplicity in the latter. It was hypothesised that energy sharing between $\tilde{\chi}_1^0$ jets and jets from, for example, squark decays was responsible for a higher than expected $\tilde{\chi}_1^0$ mass. Again, however, no correlation was seen between the $\tilde{\chi}_1^0$ mass and the smallest separation between the $\tilde{\chi}_1^0$ jets and jets from squark decays or the other $\tilde{\chi}_1^0$.

Another possibility is that there is little FSR in the SUSY events selected by this analysis. To be in the narrow slepton peak, the reconstructed $\tilde{\chi}_1^0$ momentum and mass must be close to their generated values. It is possible that events with significant FSR do not pass the selection cuts of this study. This hypothesis is strengthened by the absence in the $\tilde{\chi}_1^0$ mass peak of the low mass tails seen in the top mass distribution. The study of jet energy corrections in [10] identifies and separates the effects of ISR, FSR and hadronisation on the position of a Higgs mass reconstructed from two b-quarks. The position of the mass peak centre falls 8% when FSR is turned on and a further 10% of the Higgs mass when hadronisation is turned on.

In HERWIG, it is difficult to simply turn off FSR. If it were possible, the hypothesis of reduced FSR in the $\tilde{\chi}_1^0$ events could be tested by comparing the shifts in the $\tilde{\chi}_1^0$ and top mass peaks when FSR is turned off. If there is indeed less FSR in the SUSY events, the $\tilde{\chi}_1^0$ mass peak would be expected to shift upwards by less than the top mass peak. In the absence of this test, the ATLFAST jet energy calibration factors were reduced by 0.44; the fraction, in [10], of the downward shift of the Higgs mass peak attributed

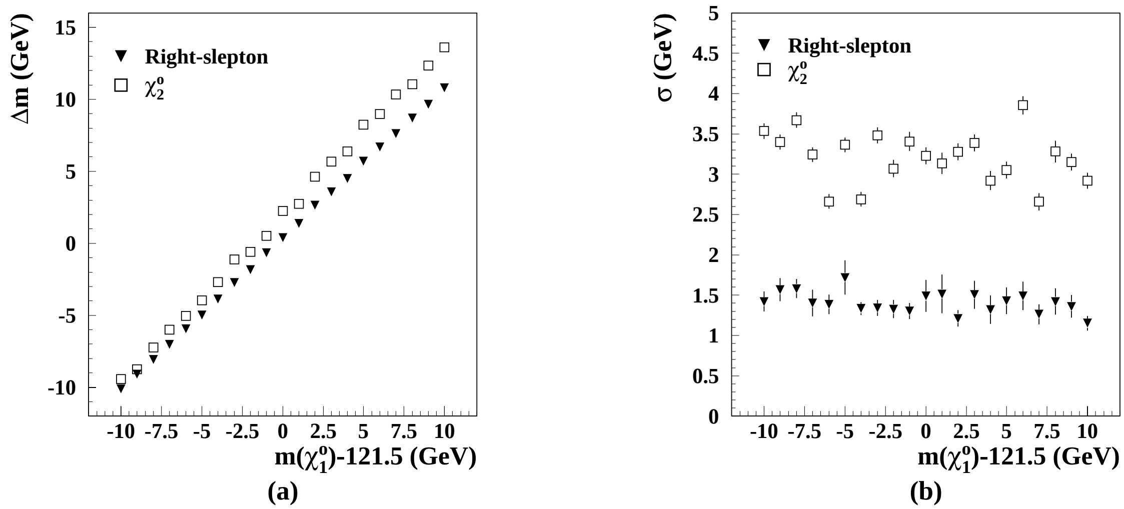

Figure 5.24: **(a)** The variation of the error on the right-slepton and $\tilde{\chi}_2^0$ masses with the difference between the true $\tilde{\chi}_1^0$ mass (121.5 GeV) and the mass, $m(\tilde{\chi}_1^0)$, assumed in jet energy correction prior to finding the slepton mass. **(b)** The width of the slepton and $\tilde{\chi}_1^0$ mass peaks plotted against $m(\tilde{\chi}_1^0)-121.5$.

to FSR. The factor of 0.968 needed to obtain a correct top mass was also applied to the $\tilde{\chi}_1^0$ jets. The resulting $\tilde{\chi}_1^0$ mass peaks for $n_{jet}^{(max)} = 10$ and $n_{jet}^{(max)} = 12$ are shown in figure 5.23. The distributions have mean values of 123.0 ± 1.2 GeV and 124.8 ± 0.6 GeV respectively. There is small shoulder in the distributions at around 160 GeV. The events in this secondary peak were found to have a wider separation between $\tilde{\chi}_1^0$ jets suggesting that any jet energy scale correction is highly dependent on process kinematics.

Using no jet energy correction, a $\tilde{\chi}_1^0$ mass of 112.5 GeV was obtained. Naïvely applying the standard ATLFAST jet calibration yields $m_{\tilde{\chi}_1^0} = 129.5$ GeV. These two values can be used to set an upper limit of $\sim$8 GeV on the systematic uncertainty in the $\tilde{\chi}_1^0$ mass. It was postulated, although not definitively demonstrated, that the ATLFAST jet calibration over-corrects the $\tilde{\chi}_1^0$ mass because of reduced FSR in the events selected by this analysis. By taking this into account, $\tilde{\chi}_1^0$ masses within 3.3 GeV of the true value were found. Given the uncertainty in the validity of this correction, the systematic error on the $\tilde{\chi}_1^0$ mass is estimated to be 5 GeV.

It is estimated that in the actual experiment, the uncertainty in the absolute jet energy scale will be of the order of 1% for jets with $p_T > 50$ GeV[17]. For lower energy jets an uncertainty of 2-3% is more likely. With real data, therefore, it may be possible to reduce the systematic uncertainty on the $\tilde{\chi}_1^0$ mass to 2% (2.4 GeV).

Slepton and $\tilde{\chi}_2^0$ mass measurement systematics

Before finding slepton and $\tilde{\chi}_2^0$ masses in section 5.6.6, a correction was applied to the 4-momenta of the jets from the $\tilde{\chi}_1^0$ decay. After this correction, the mass of all reconstructed $\tilde{\chi}_1^0$s is equal to the true mass and the width and bias of the mass peak are removed. A similar procedure would be followed in the actual experiment but the true mass would be unknown. Instead, the $\tilde{\chi}_1^0$ jets will be calibrated so that all $\tilde{\chi}_1^0$ masses are equal to the best estimate of the true mass. In the previous section, a systematic error of 5 GeV on the $\tilde{\chi}_1^0$ mass measurement was found. This error introduces a systematic error into the measurement of the slepton and $\tilde{\chi}_2^0$ masses.

Figure 5.24 shows an approximately linear variation of the errors on the slepton and $\tilde{\chi}_2^0$ masses with the error in the $\tilde{\chi}_1^0$ mass. The uncertainty in the jet energy scale will therefore contribute a systematic error of approximately 5 GeV to the slepton and $\tilde{\chi}_2^0$ masses.

A second contribution to the $\tilde{\chi}_2^0$ and slepton mass systematic is the uncertainty in the absolute lepton momentum scale. At the TeVatron this scale is known to approximately 0.1%. Work in [17] shows that an error of 0.02% in the electron momentum scale is possible. The systematic error on the muon momentum scale, however, will probably be closer to 0.1%. For the purposes of this analysis, a systematic error of 0.1% is used for both leptons. The average transverse momentum of the leptons is approximately 70 GeV (figure 5.12) and the systematic error on the momentum is therefore of order 0.1 GeV. It is assumed that the error on the angular measurement of leptons is small compared to the momentum systematic.

5.7 Conclusions

The majority of ATLAS SUSY studies have concentrated on R-parity conserving models. There are, however, no theoretical or empirical reasons to impose R-parity conservation. This chapter presents a study of mSUGRA point 5 with a non-zero RPV coupling, $\lambda''_{212} = 0.005$. The study is the first to use a new version of the HERWIG event generator which correctly incorporates RPV vertices. The ATLAS detector is simulated using ATLFAST, a well tested particle level simulation.

The small RPV coupling of this study allows the LSP ($\tilde{\chi}_1^0$) to decay via a baryon number violating vertex into a charm, a down and a strange quark. It has been demonstrated that a $\tilde{\chi}_1^0$ mass peak can be found after three years of low luminosity running using cuts on jet kinematics and multiplicity and a statistical background subtraction. No flavour tagging of jets is used and the algorithm is therefore equally applicable to other RPV λ'' couplings. In fact, the algorithm could, in principle, be modified to find the $\tilde{\chi}_1^0$ mass in a variety of mSUGRA scenarios.

If the decay chain $\tilde{\chi}_2^0 \to \tilde{l}_R^{\pm} l^{\mp} \to l^{\pm} l^{\mp} \tilde{\chi}_1^0$ is open, as at point 5, a significantly improved $\tilde{\chi}_1^0$ mass peak with minimal background can be obtained. It was also shown that the masses of the light right-sleptons and the $\tilde{\chi}_2^0$ can be measured. The errors on these measurements were found to be dominated by the systematic uncertainty in the jet energy scale. Table 5.13 summarises the masses found and the associated errors.

Sparticle	True mass (GeV)	Measured mass (GeV)
$\tilde{\chi}_1^0$	121.5	124.8 ± 0.6(stat)± 5.0(had)
Right-smuon/selectron	157.2	157.6 ± 0.02(stat)± 5.0(had)± 0.1(EM)
$\tilde{\chi}_2^0$	233.0	235.6 ± 0.2(stat)± 5.0(had)± 0.1(EM)

Table 5.13: A summary of the masses found in this analysis and the statistical and systematic errors on each measurement. The systematic errors from hadronic (had) and electromagnetic (EM) calorimetry are shown separately.

Bibliography

[1] S Martin. A Supersymmetry Primer. In G.L. Kane, editor, *Perspectives on Supersymmetry*. World Scientific, 1999. Extended version available as hep-ph/9709356.

[2] MSSM Working group. Report of the MSSM working group for the Workshop "GdR-Supersymétrie". PM/98-45, 1998.

[3] L Alvarez-Gaumé et al. Minimal low-energy supergravity. *Nucl. Phys. B*, 221:495–523, 1983.

[4] I Hinchcliffe et al. Precision SUSY Measurements with ATLAS: Introduction and Inclusive Measurements. ATLAS Internal Note PHYS-97-107, CERN, 1997.

[5] ATLAS Collaboration. ATLAS Detector and Physics Peformance TDR, Volume II. Technical Report CERN/LHCC 99-15, CERN, 1999.

[6] H Dreiner. An Introduction to Explicit R-parity Violation. In G.L. Kane, editor, *Perspectives on Supersymmetry*. World Scientific, 1997. hep-ph/9707435.

[7] C. Caso et al. 1998 Review of Particle Physics. *The European Physical Journal C3*, 1, 1998.

[8] G Bhattacharyya. A brief review of R-parity violating couplings. *hep-ph/9709395*, 1997.

[9] A Mirea & E Nagy. Study of the determination of the SUGRA parameters using the ATLAS detector in the case of L-violating R parity breaking. Internal ATLAS note PHYS-99-007, CERN, 1999.

[10] E Richter-Was et al. ATLFAST 2.0: A Fast Simulation Package for ATLAS. ATLAS Internal Note PHYS-98-131, CERN, 1998.

[11] G Marchesini et al. HERWIG 5.9. *Computer Phys. Commun.*, 67:465, 1992.

[12] K Odagiri. HERWIG 6.1, with supersymmetric processes. Talk given at The Second Workshop: Tools for SUSY '99, Lyon, March 31st - April 2nd, 1999.

[13] H Dreiner & P Richardson. R-Parity Violating Monte Carlo Simulations with HERWIG. Talk given at The Second Workshop: Tools for SUSY '99, Lyon, March 31st - April 2nd, 1999.

[14] H. Baer et al. Simulating Supersymmetry with Isajet 7.0/Isasusy 1.0. *hep-ph/930329*, 1993.

[15] B Allanach et al. Stringy SUSY searches at the LHC. To be published.

[16] ATLAS Collaboration. ATLAS Calorimeter Performance TDR. Technical Report CERN/LHCC 96-40, CERN, 1996.

[17] ATLAS Collaboration. ATLAS Detector and Physics Peformance TDR, Volume I. Technical Report CERN/LHCC 99-14, CERN, 1999.

[18] E. Buis et al. Parameterisation of the Inner Detector Performance. ATLAS Internal Note INDET-98-197, CERN, 1998.

[19] ATLAS Collaboration. ATLAS Inner Detector TDR, Volume I. Technical Report CERN/LHCC 97-16, CERN, 1997.

[20] D Cavalli & S Resconi. Comparison between full simulation and fast simulation of the ATLAS detector. ATLAS Internal Note PHYS-97-100, CERN, 1997.

[21] H Baer et al. Impact of hadronic decays of the lightest neutralino on the reach of the CERN LHC. *Phys rev D*, 55:1466–1470, 1997.

[22] J Söderqvist. Consequences of Baryonic R-parity Violation for Measurements of SUSY Particles using the ATLAS Detector. ATLAS Internal Note PHYS-98-122, CERN, 1998.

[23] M Bosman et al. Jet Finder Library: Version 1.0. ATLAS Internal Note SOFT-98-038, CERN, 1998.

[24] G Polesello et al. Precision SUSY measurements with ATLAS for SUGRA point 5. ATLAS Internal Note PHYS-97-111, CERN, 1997.

[25] H Baer et al. Cosmic relic density from minimal supergravity with implications for collider physics. *Phys. Rev D.*, 53:597–605, 1996.

[26] ALEPH, DELPHI, L3 and OPAL Collaborations. Limits on Higgs boson masses from combining the data of four LEP experiments at $\sqrt{s} \leq 183$ GeV. EP 99-060, CERN, 1999.

[27] Higgs Working Group. Physics at LEP2: Higgs Physics. Yellow Report 96-01, CERN, 1996.

[28] E Richter-Was & D Froidevaux. MSSM Higgs searches in multi-b-jet final states. ATLAS Internal Note PHYS-97-104, CERN, 1997.

[29] P Savard. The $W \rightarrow$jet-jet and top mass reconstruction with the ATLAS Detector. ATLAS Internal Note CAL-97-092, CERN, 1997.